UNIVERSITY OF SOUTHAMPTON

SPIN RELAXATION PHENOMENA IN GaAs/AlGaAs QUANTUM WELLS

By

GARETH JOHN

A thesis submitted for PhD at the School of Physics and Astronomy

2005

UNIVERSITY OF SOUTHAMPTON

ABSTRACT.

SCHOOL OF PHYSICS OF ASTRONOMY

Doctor of Philosophy

SPIN RELAXATION PHENOMENA IN GaAs/AlGaAs QUANTUM WELLS

By

GARETH JOHN

This thesis presents a study of carrier dynamics in GaAs/AlGaAs quantum wells. Non-equilibrium distributions of spin polarisations were excited and probed in wells grown in (100) and (110) crystal orientations by means of picosecond pulses. This spin polarisation decays exponentially with time and can be understood in terms of a motional narrowing scattering process described by D'yakonov and Perel, concerning the effect of spin splitting of the conduction band creating a fictious magnetic field that acts upon the spin of the electron. These scattering processes can also include electron-electron scattering events that do not contribute to the mobility.

The (110) wells were studied to show the effect of both built in and applied bias on the spin relaxation time. It was thought that this contribution to the mean square precession frequency of the electron would act at right angles to the spin splitting of the conduction band and hence increase the rate of spin relaxation. Calculations were made of the theoretical values of spin relaxation as a function of applied bias and these values were compared with experimental values. It was necessary to assume less than optimum growth conditions in order to account for the discrepancies at low bias. A (110) sample was also investigated for magnetic field dependence in order to derive a value for the momentum scattering time but the results remain inconclusive.

(100) samples were investigated to study the expected occurrence of a minimum in the temperature dependence of the spin relaxation rate, corresponding to the Fermi temperature. This sample was also investigated to study the carrier concentration dependence of the spin relaxation rate. At low biases neutral and negatively charged excitons were seen and deductions were made about their spin relaxation.

This thesis is dedicated to my father.

Acknowledgements

Many people have contributed to my time at the School of Physics. In particular I would like to thank Professor Richard Harley for supervision and guidance over the years; Matthew Brand for the encouragement to keep going when I was considering giving up: Greg Stevens for the same; and Oleg Karimov for showing me how to use a laser lab. I would also like to thank Tom Perkins for all the invaluable technical support he has given over the past four years and as Colin Miles for all his help.

I would also like to thank my family and all the people at the Forty Pounds Players, whose encouragement made this all possible.

CONTENTS

CHAPTER 1

INTRODUCTION

This thesis examines the dynamics of electron spins in certain III-V heterostructures. A low dimensional heterostructure is one in which the motion of an electron is confined in one or more directions to the order of the de Broglie wavelength. (1,2). Two such structures are dealt with, namely two dimensional electron gases (2DEGS) and (110) oriented quantum wells. The investigative method involved manipulation of the spins using a pico-second time-scale optical pump-probe technique. The change in the spin state over time is dependent upon a variety of factors. The dependences on temperature, built in and applied electric field, heterostructures growth direction and carrier concentration are discussed in detail.

The main focus of this project is on testing fundamental quantum physical theories of electron spin dynamics in semiconductors. Nevertheless, the areas chosen are relevant to and therefore underpin possible spintronic devices and technologies. The work in hand is mostly concerned with the scattering mechanisms experienced by carriers and their relationship to spin polarisation.

Three pieces of experimental work are detailed in this thesis.

In the first set of measurements a sample containing quantum wells grown in the (110) direction was studied. In this case the spin relaxation time was expected to be significantly longer than in the (100) case. A strong dependence on built-in and applied electric field was also expected. Both of these expectations are borne out and the general agreement with the theory is good. The results were compared with theoretical values derived from a non-perturbative numerical calculation and an attempt is made to explain discrepancies between the calculated and experimental

values with reference to the different spin relaxation mechanisms involved. The influence of interface roughness of the quantum well on the spin precession is also discussed.

In the second and third sets of measurements, spin relaxation was investigated for electrons in a high mobility 2DEG in a 100Å AlGaAs/GaAs quantum well in order to test the theoretical predictions of the importance of electron-electron scattering. Electron concentration was varied by means of a semi-transparent gate electrode and mobility was determined from Hall effect measurements. Measurements of the spin relaxation time have been taken at temperatures between 10K and 275K to investigate the expected occurrence of a minimum in the spin relaxation rate. It is thought that the spin relaxation rate shows a minimum in the vicinity of the Fermi temperature T_F. At this point the electron system changes from a degenerate to a non-degenerate state. The data does show a minimum at ~70K, close to the expected value of $T_F \approx 70K$.

The third set of measurements was an investigation of the spin relaxation rate as a function of carrier concentration. These were performed on the same sample as noted above. The theoretical predictions were very different for temperatures above and below T_F: $T < T_F$, $\tau_s^{-1} \sim N_S^2$ and when $T > T_F$, $\tau_s^{-1} \sim N_S^{-1}$. This was not wholly successful as it was found that neutral and negatively charged excitons are soon formed in the well as the concentration is reduced below the maximum value available for the sample geometry. Measurements were made of the spin dynamics of both neutral and negatively charged excitons.

CHAPTER 2

THEORETICAL BACKGROUND

This chapter will detail the dynamics of electrons in a direct band gap non-centrosymmetric semiconductor, in this case GaAs. Attention will be paid to the properties of GaAs with regard to spin polarisation. The direct band gap means that the spin polarisation of electrons in GaAs can be selected optically through polarisation of the light. The change in band structure and optical coupling to the bands as the dimensionality of the structure is reduced will also be dealt with. Restricting the degrees of freedom of the electrons also has profound implications for scattering mechanisms that affect the spin relaxation time.

2.1 Band structure of GaAs.

The behaviour of charge carriers in a semiconductor can be understood by examining the band structure.

A simple model of the band structure of the direct band gap semiconductor GaAs consists of one conduction band and three valence bands as shown in figure 2.1a. Zincblende structures such as GaAs lack inversion symmetry. This inversion asymmetry creates a spin splitting of the conduction and valence bands, that is, the conduction band's degeneracy is lifted and the spin up and spin down states have different energy levels; spin up and spin down electrons have different energies when in the same momentum state. Three valence bands exist because of the p-orbital nature of the band. For p-orbitals the angular momentum quantum number L = 1 so $m_L = +1, 0$ or -1. This creates three levels, known as light hole, heavy hole and a split off band caused by the spin orbit interaction. The terms light hole and heavy hole refer to the curvature of the dispersion of these bands. The hole energy levels are

doubly degenerate at **k**=0 and this degeneracy is lifted at **k**≠0. The holes have a z-component of angular momentum of J_z= ±1/2 and J_z= ±3/2 for light and heavy holes respectively. [1, 2, 3].

In a quantum well the charge carriers are confined in a potential well. This potential acts as a perturbation on the bands and lifts their degeneracy, as shown in figure 2.1.

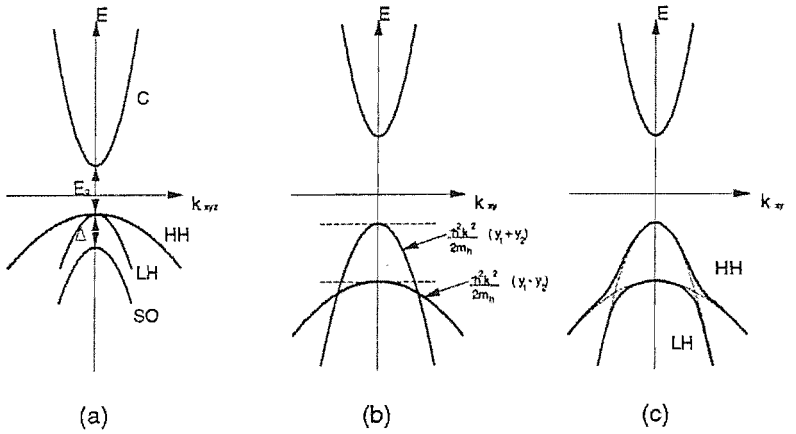

Figure 2.1 (a). The conduction (C) and valence bands in bulk zincblende semiconductor, showing the light hole (LH), heavy hole (HH) and spin orbit (SO) split off bands. (b) The band crossing predicted in the quantum well case. (c) The anticrossing produced by introducing higher order terms into the perturbation. Excerpted from Worsley, (1995).[14]

Figure 2.2b shows the dispersion for wavevectors in the quantum well plane. For this case it appears, from the curvature of the bands, that the higher valence heavy hole band has a lighter effective mass than the lower, light hole band at **k**=0. However, the order of the bands is determined by the effective masses for motion perpendicular to the plane and for this case it is clear that the heavy hole band has the lesser confinement energy consistent with a greater effective mass. Once higher order terms of the **k.p** perturbation are introduced, there is an anticrossing of the bands,

which leads to an increase in the heavy hole mass and a corresponding decrease in the light hole mass (figure 2.2c). The influence of quantum confinement on the bands means that the separation of the bands, and hence confinement energy of light holes, heavy holes and electrons, can be controlled by varying the well width L_z and the barrier height. The separation of the bands allows selective excitation of electrons from the valence bands at the zone centre $\mathbf{k}=0$ so that experiments may be performed with 100% spin polarisation of excited particles. [1, 2, 3.]

2.2 Optical Selection Rules.

Electrons can make optically induced transitions between the bands. These transitions are governed by selection rules. In addition to conservation of energy and crystal momentum, the transitions of electrons optically excited from the valence to conduction bands follow selection rules that conserve the angular momentum of the photon absorbed in the transition, as in indicated figure 2.2. When a circularly polarised photon is absorbed, its angular momentum is transferred to an electron, creating an electron hole pair with total spin angular momentum equal to that of the photon. If the photon is left or right circularly polarised the electron hole pair carries an angular momentum of +1 or −1 respectively, in units of $\hbar$.

The absorption probabilities for electrons excited from the light and heavy hole bands differ by a factor of three and, as a result, in bulk GaAs, the absorption of right circularly polarised light creates a net spin polarisation of conduction band electrons of 50%. This process is known as optical pumping or optical spin polarisation. It is important not least because it allows for the study of spin polarisation without the need for electronic spin injection. Recombination of electron hole pairs produces a circularly polarised photon. This means that the spin

polarisation of the electron can be detected from the polarisation state of the emitted photon. [1, 2, 3.]

When the 2-D case is considered, the light and heavy hole levels are no longer degenerate at the zone centre and 100 % polarisation states can be more easily selected. The splitting between light and heavy hole subbands increases with decreasing well width L_z, as does the conduction band confinement energy. The difference in energy levels between the bulk and 2D case can be seen in figure 2.2.

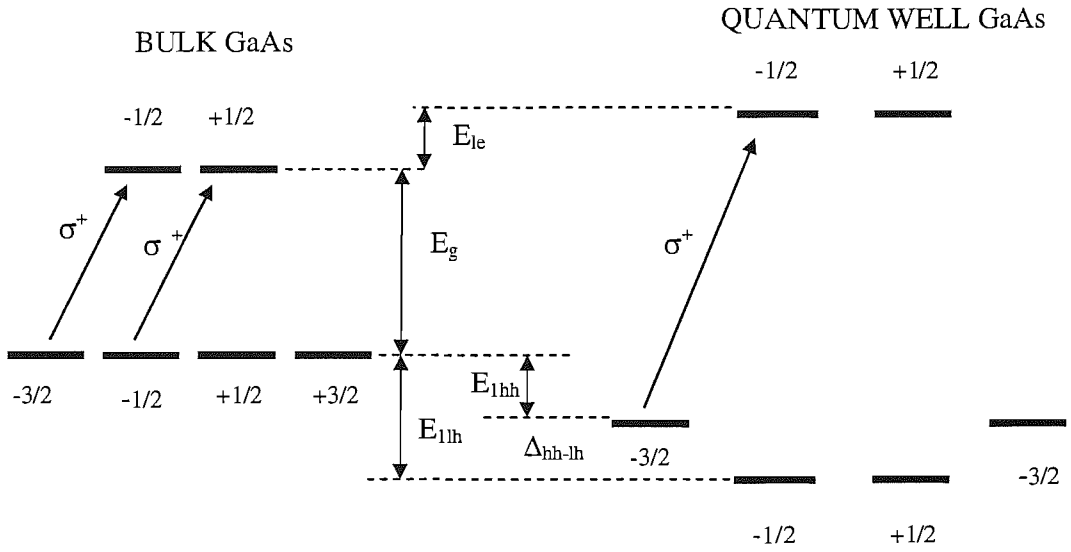

Figure 2.2. Optical selection rules at **k**=0 for bulk and quantum well GaAs. E_g is the band gap of bulk GaAs, E_{le}, E_{lhh} and E_{llh} are the confinement energies of the conduction electron and the light and heavy hole valence band states. $\Delta_{hh\text{-}lh}$ is the splitting of the light and heavy hole states when the degeneracy is lifted by quantum confinement. The numbers on the energy levels represent the z-component of the angular momentum and the σ^+ on the arrows show the transitions caused by left circularly polarised light between the energy levels that are allowed by the optical selection rules.

2.3 Spin Relaxation Mechanisms.

The optical selection rules discussed in section 2.2 can be exploited to generate spin polarised populations of electrons, holes and also excitons, which may contribute to the observed spin dynamics, depending upon the timescale of

observations and the experimental conditions. In this thesis we are interested mainly in the spin dynamics of conduction electrons. Generally the hole populations lose spin orientation on a timescale much shorter than electrons because of the strong spin orbit admixture in the valence band states. Exciton formation is not important in our measurements on (110) oriented quantum wells at temperatures above 100K and only becomes significant in our measurements on 2DEGs for relatively low electron concentrations.

There are three spin relaxation mechanisms for conduction electrons to be considered in the course of this thesis.

The Bir-Aronov-Pikus (BAP) spin relaxation mechanism involves spin flips of electrons scattering from free or bound holes (figure 2.3). This mechanism only occurs in cases where the material has significantly high concentrations of holes and when the hole gas has essentially zero spin polarisation. In general this mechanism can be neglected in intrinsic or n-type systems such as those we have investigated in this thesis. [4]

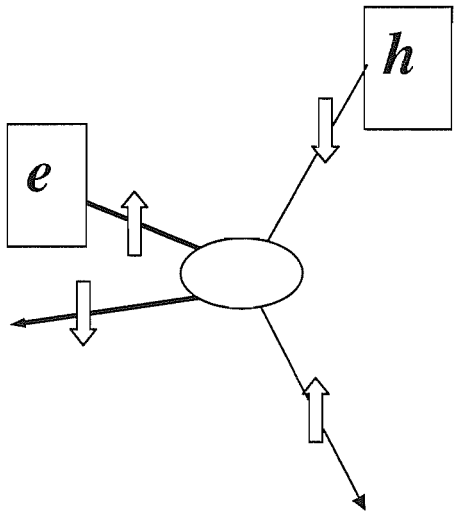

Figure 2.3. Bir-Aronov-Pikus spin relaxation mechanism. The oval represents an electron scattering event from a free or bound hole which results in an electron spin flip.

The Elliott-Yafet (EY) mechanism considers coupling between the conduction and valence band states that can lead to admixture of spin-up and spin-down conduction bands leading to spin flips simultaneous with momentum scattering, induced by spin orbit relaxation. [5,6] (see figure 2.4). There are two reasons why this mechanism is negligible in the systems we study here. Firstly, it turns out that the intrinsic strength of the spin-flip scattering process envisaged is considerably less than that of the spin-precession in-flight considered in the third mechanism discussed below. Secondly, it results in a spin relaxation rate proportional to the momentum scattering rate so that it becomes unimportant in high quality samples.[7]

.

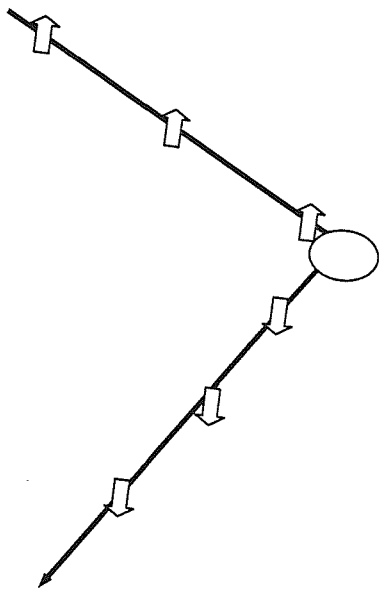

Figure 2.4. Elliott Yafet spin relaxation mechanism. The oval represents a momentum scattering event that induces a spin flip. This is caused by coupling between the conduction and valence band states

The third mechanism, known as the D'yakonov-Perel (DP) mechanism, involves the spin orbit splitting of the conduction band of GaAs mentioned in the previous discussion. This is the dominant relaxation mechanism in

much of the work under discussion (see figure 2.5). The spin splitting may be thought of as an effective magnetic field acting upon the spin part of the electron wave function [8], each momentum state has its own magnetic field, which causes precession of the spin through the equation of motion $d\mathbf{S}/dt = \mathbf{S} \times \mathbf{B}(\mathbf{k})$.

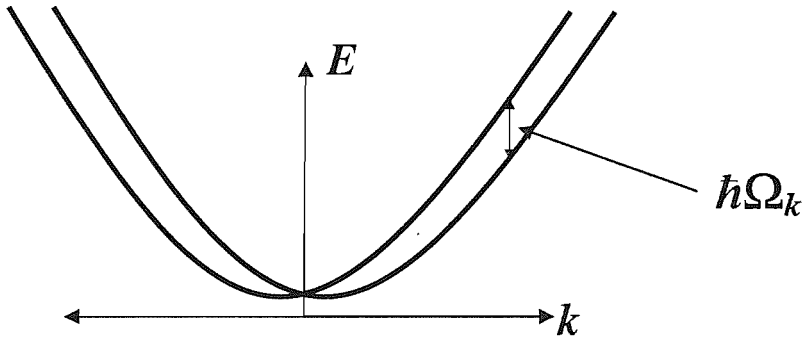

Figure 2.5. Spin splitting of the conduction band in a zincblende structure.

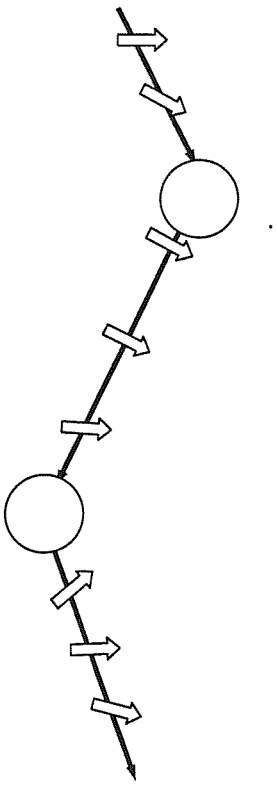

Figure 2.6. D'yakonov Perel Spin Relaxation. Each circle represents a scattering event that halts and then reorients the precession of the electron spin. The electron continues to precess after the scattering event but about a new axis appropriate to the new momentum.

Consider an electron with momentum $\hbar\mathbf{k}$. The electron spin will precess about the direction of the effective internal magnetic field. Assuming that momentum scattering is strong, as is usually the case, before the electron spin has moved through a large angle, it will experience a collision (from impurities, lattice defects, other electrons) and be scattered to another momentum state $\hbar\mathbf{k}'$. Such fractional rotations of the spin vector are shown schematically in figure 2.6. Scattering causes a randomly changing precession direction and precession frequency for the electron spin which therefore reorients through a random walk process described by the equation:

$$\tau_s^{-1} = \langle\Omega^2\rangle\tau_p^* \qquad (2.1)$$

where τ_s^{-1} is the spin relaxation rate, $\langle\Omega^2\rangle$ is the mean square precession frequency and τ_p^* is the momentum relaxation time [1].

In the original interpretation, τ_p^* was thought to be the same as the transport relaxation time τ_p that in turn determines the mobility. [9] This is not now thought to be the case, as collisions that do not affect the mobility do affect spin precession. [11, 12, 13]. This will be dealt with in more detail in chapter 6. D'yakonov and Kachorovskii [10] later extended this theory to deal with the effects of quantum confinement. This is known as the D'yakonov-Perel- Kachorovskii spin relaxation mechanism, and is dealt with in the following section.

2.3.1 Effect of growth direction of quantum well on the DP mechanism.

In a crystal with inversion asymmetry and spin orbit coupling the spin splitting is described by the Hamiltonian:

$$H = \hbar\Omega_k \cdot \sigma/2 \qquad (2.2)$$

where Ω_k is the spin precession vector and σ is the Pauli matrix. The spin precession vector has three components:

$$\Omega_x = k_x(k_y^2 - k_z^2) \qquad (2.3a)$$

$$\Omega_y = k_y(k_z^2 - k_x^2) \qquad (2.3b)$$

$$\Omega_z = k_z(k_x^2 - k_y^2) \qquad [10] \quad (2.3c)$$

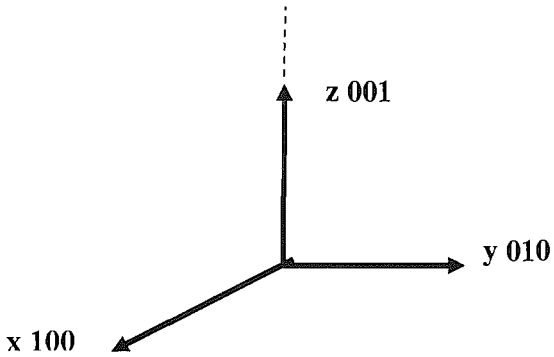

Figure 2.7. The principal axes and growth axis of a (100) quantum well. The growth axis is represented by the dotted line.

When a (001) quantum well is formed, the k vector is quantised in the z direction. (See figure 2.7.) Therefore, the most significant terms in equation 2.3 are determined where k_z is replaced by the expectation value $\langle k_z \rangle$ and k_z^2 by the expectation value $\langle k_z^2 \rangle$. $\langle k_z \rangle$ is equal to zero, however $\langle k_z^2 \rangle \neq 0$. The value of $\langle k_z^2 \rangle$ becomes larger as the width of the well is reduced. The leading components become:

$$\Omega_x \sim -k_x \langle k_z^2 \rangle + (k_x k_y^2)$$

$$\Omega_y \sim k_y \langle k_z^2 \rangle - (k_y k_x^2)$$

and the z component $\Omega_z \alpha \langle k_z \rangle (k_x^2 - k_y^2) = 0$

The terms in brackets in the x and y cases are small and can be ignored at all but high temperatures. Therefore, in the case of a quantum well grown in the (001) direction, the internal field that drives spin relaxation is in the xy plane of the well. This leads to rapid spin relaxation for spin component along the growth axis.[10]

In the case of a quantum well grown in the (110) direction, the derivation is more complicated as the growth axis does not lie along one of the principal axes of the well. (See figure 2.8).

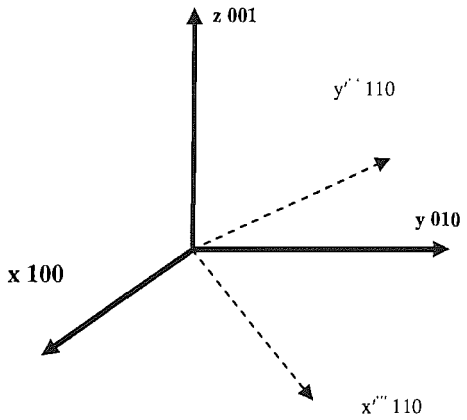

Figure 2.8. Principal axes and growth axes of the (110) quantum well. The growth axis is x′ (110)

In this case it is necessary to project each component of the spin precession vector (equation 2.3) onto the principal axes. (The primes correspond to the projection of the k vector onto the (110) and (110) axes $k_x = k_x' - k_y'$, $k_y = k_x' + k_y'$)

$$\Omega_x \sim (k_x' - k_y')(k_x'^2 + k_y'^2 + 2k_x'k_y' - k_z^2)$$

$$\Omega_y \sim (k_x' + k_y')(-k_x'^2 - k_y'^2 + 2k_x'k_y' + k_z^2)$$

$$\Omega_z \sim 2k_zk_x'k_y'$$

The projection of each component onto the x' and y' axes is:

$$\Omega_x' \sim \Omega_x + \Omega_y = 2k_y'(k_x'^2 - k_y'^2 + k_z^2)$$

$$\Omega_y' \sim -\Omega_x + \Omega_y = 2k_x'(-k_x'^2 + k_y'^2 + k_z^2)$$

The wavefunction is quantised in the x′ (110) direction. Therefore, we replace k_x' and $k_x'^2$ by $\langle k_x' \rangle = 0$ and $\langle k_x'^2 \rangle \neq 0$, giving $\Omega_x' = 2k_y' \langle k_x' \rangle$ and $\Omega_y' = \Omega_z = 0$. Therefore, the spin precession vector is oriented in the growth direction of the well i.e. , perpendicular to the plane of the well. This leads to much longer (in principle infinite) spin relaxation times for polarisation along the growth direction of a (110) well compared to those in a (100) well. [10]

The contribution to the spin splitting of the conduction band just considered arises from the inversion asymmetry of the zincblende lattice, and is known as the Bulk Inversion Asymmetry (BIA) or the Dresselhaus term. Two further sources of inversion asymmetry contribute terms to the spin splitting in quantum wells. Firstly, inversion asymmetry associated with the quantum well structure, for example from applied electric field or built in asymmetry of barriers is known as Structural Inversion Asymmetry (SIA). This will be discussed in chapter 5. Secondly, asymmetry of the interfaces themselves where there are different atomic species at the well's interfaces. This is known as Native Interface Asymmetry (NIA.) This effect is only significant where both atomic species change at the interface. As this project involves GaAs/AlGaAs wells the NIA contribution to spin splitting is negligibly small and will not be considered further.

2.4 References.

1. "Optical Orientation," edited by F. Meier and B.P. Zakharchenya, North-Holland, Amsterdam (1984).
2. "Quantum Semiconductor Structures, Fundamentals and Applications," C. Weisbuch and B. Vinter, Academic Press Inc., Boston. (1991).
3. "Ultrafast Spectroscopy of Semiconductors and Semiconductor Nanostructures," J. Shah, Springer, Berlin, (1999).
4. "Spin Relaxation of electrons due to scattering by holes," G.L. Bir, A.G. Aronov and G.E. Pikus, Sov. JETP, **42** 705 (1976).
5. "Theory of the effect of spin-orbit coupling on magnetic resonance in some semiconductors," R. J. Elliottt, Phys. Rev. **96** 266 (1954).
6. "g-factors and spin-lattice relaxation of conduction electrons," Y. Yafet, Solid State Phys. **14** 1 (1963).

7. "Investigation of narrow-band semiconductor quantum well structures using a synchronously-pumped optical parametric oscillator," P.A. Marsden, PhD. Thesis, University of Southampton (2001).
8. "Spin-orbit coupling effects in zincblende structures," G. Dresselhaus, Phys. Rev. **100** 580 (1955).
9. "Spin relaxation of conduction electrons in noncentrosymmetric semiconductors," M. I. D'yakonov and V. I. Perel, Sov. Phys. JETP **33** 1053 (1971).
10. "Spin relaxation of two-dimensional electrons in noncentrosymmetric semiconductors," M. I. D'yakonov and V. Yu. Kachorovskii, Sov. Phys. Semicond. **20** 110 (1986).
11. "Precession and motional slowing of spin evolution in a high-mobility two-dimensional electron gas," M. A. Brand, A. Malinovski, O. Z. Karimov, P. A. Marsden, R. T. Harley, A. J. Shields, D. Sanvitto, D. A. Ritchie and M. Y. Simmons. Phys. Rev. Lett. **89** 239901 (2002).
12. "Precession spin relaxation mechanism caused by frequent electron-electron collisions," M. Glazov and E. L. Ivchenko, JETP Letters, **75** 403.
13. "D'yakonov-Perel spin relaxation under electron-electron collisions in n-type QWs," M. Glazov, E. L. Ivchenko, M. A. Brand, O. Z. Karimov and R. T. Harley,
14. Worsley, R.E. "Time Resolved Relaxation processes in Quantum Wells." PhD thesis, University of Southampton, 1995.

CHAPTER 3

TIME RESOLVED MEASUREMENT METHOD.

3.1 Introduction

The continuous wave (CW) laser can glean a great deal of information about quantum wells. For instance, photoluminescence (PL) and photoluminescence excitation (PLE) measurements are used to determine the band gap and the depth of the Fermi sea in the conduction band of a quantum well, as shown in figure 3.1.

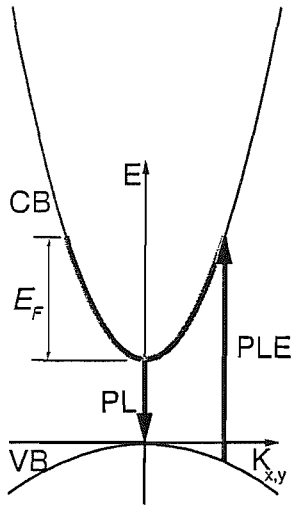

Figure 3.1. The band structure of a direct band gap semiconductor. The PL gives the energy gap E_g and the PLE measurement gives a value for the depth of the Fermi sea.

Estimates of spin relaxation time can also be gained from the Hanle effect technique using the CW laser, but this is only an indirect measurement of the dynamic processes involved. For direct measurements a modelocked (pulsed) laser source is necessary. This allows direct measurement of carrier lifetime and spin relaxation time. In the pump probe technique adopted here, laser pulses of ~2 ps duration (known as the pump beam) are used to excite a non-equilibrium distribution of electrons into the

conduction band. A second, weaker test pulse (known as the probe beam) is focused on the same spot on the sample and its reflected intensity and polarisation examined. The signal obtained by comparing the reflected intensity with the incident intensity of the probe beam gives the carrier lifetime and is known as the sum signal. The signal from the reflected beam obtained by observing the rotation of the plane of polarisation of the reflected probe gives the spin relaxation time and is known as the difference signal.

3.2 History of the Time Resolved (TR) method.

This section will summarise the different variations of the pump probe method used in this group and explain how the current method was arrived at. Sources of error in the current method will also be examined.

An early system used for TR employed crossed polarisers in the path of the incident and reflected probe beams. The polarisers could be adjusted so that there was a null signal in the absence of the pump beam. Therefore, any pump induced rotation of the polarisation would result in a signal. However, pump induced ellipsation would also induce a signal. To discriminate between rotation and elliptisation the polarisers were uncrossed by a few degrees. This method had reasonable sensitivity but suffered from noise associated with fluctuations in the power of laser that were imprinted directly on the signal.

This technique was supplanted by using a photoelastic modulator (PEM) to analyse the rotation of the reflected probe beam. A photomultiplier tube was used to amplify the signal before it was analysed using two lock-in amplifiers. (See figure 3.2.)

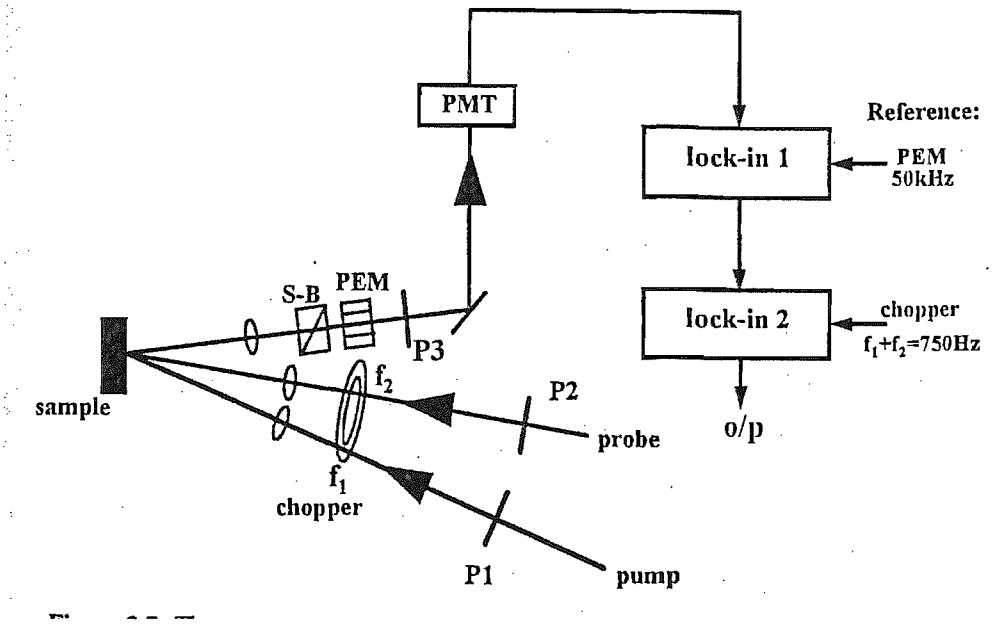

Figure 3.2. Photoelastic modulator (PEM) set up for time resolved measurements. Excerpted from Gravatt, 1988 [1].

The PEM and polarizer P3 act as a time-dependent filter transmitting alternately left and right polarised light at a frequency of 50 kHz. The lock-ins were configured to measure either the pump-induced difference of the two polarisations or the change in intensity of the probe beam. To obtain the polarisation difference the first lock-in was referenced at 50 kHz for the PEM while the second was referenced at the sum of the chopping frequencies (f_1+f_2) of the pump and probe beams in order to separate scattered pump intensity from the probe beam. The time constant of lock-in 1 was set to be less than $(f_1+f_2)^{-1}$. To obtain the pump-induced change of intensity of the probe beam lock-in 1 was bypassed. Although this technique was used with some success [1] it did contain certain disadvantages, which led to its use being discontinued. For instance, the low quantum efficiency of the PMT meant that the system had low sensitivity and, as before, laser intensity fluctuations translated directly to noise in the signal. [1].

It was because of these problems that the balanced detection system described in the next section was developed.

3.3 The Balanced Detection System.

The balanced detection system relies upon two pairs of silicon pin photodiodes to measure the sum and difference signals. This has the advantage of allowing common mode noise rejection and great sensitivity to the reflected probe beam.

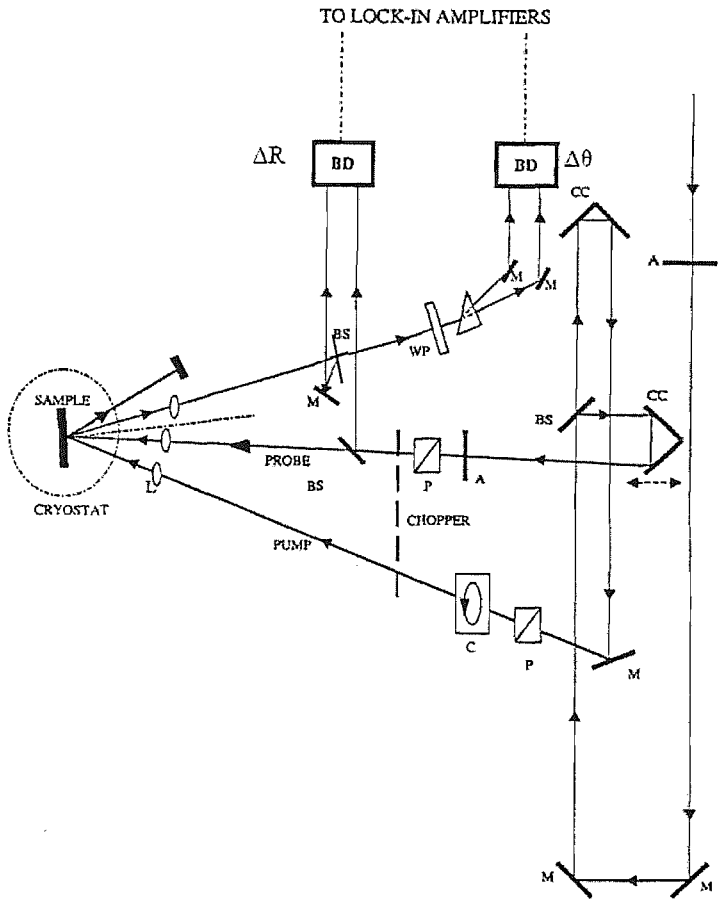

Figure 3.3. Balanced detection set up for time resolved measurements.

In this set up (shown in figure 3.3) the beam from the mode locked Ti: sapphire laser (Coherent Radiation MIRA) is attenuated using the variable neutral density filter A. An arrangement of beam splitters, a mirror and two corner cubes split the beam into pump and probe beams. To set the circular polarisation of the pump beam a Soleil Babinet compensator (C) was used. The probe beam is attenuated by a variable neutral density filter (A) until its intensity is a fraction of the probe beam (typically $1/5^{th}$) and set for linear polarisation by a polariser P. Each beam is then chopped at a different frequency and then focussed on the sample by lenses. The reflected pump beam is blocked and the probe beam is collimated by a third lens. The reflected beam then passes through a beam splitter, set almost normal to beam direction in order to avoid polarisation sensitivity of the reflected component. This component is then reflected by mirror M into one photodiode of the first balanced detector BD. The other photodiode receives a reference component, selected by a beam splitter BS inserted into the probe beam between the chopper and the sample. The balance detector subtracts the current of one photodiode from the other. The remaining current goes to one channel of the lock in as the sum signal, ΔR. A variable neutral density filter in the reference beam is used to balance the photodiode signals so that there is no signal when there is no optical pumping.

The component of the beam that passes through BS then passes through a half wave plate (WP) followed by a birefringent prism which has its optic axis parallel to the apex. The prism therefore separates the beam into e- and o- rays which are incident on the two balanced photodiodes by reflection from the mirrors M. the balanced detector then subtracts the current of one photodiode from the other and this is sent to the second channel of the lock-in as the difference signal, $\Delta\theta$.

The detectors have to be balanced so that there is no signal without the pump beam. Rotation of the half wave plate will produce an exact balance of the signals with the pump beam blocked, as illustrated in figure 3.4. The left hand panel shows the chopped signal from the two photodiodes with the half wave plate slightly misoriented and the right hand panel shows exact balance achieved by correct adjustment of the half wave plate.

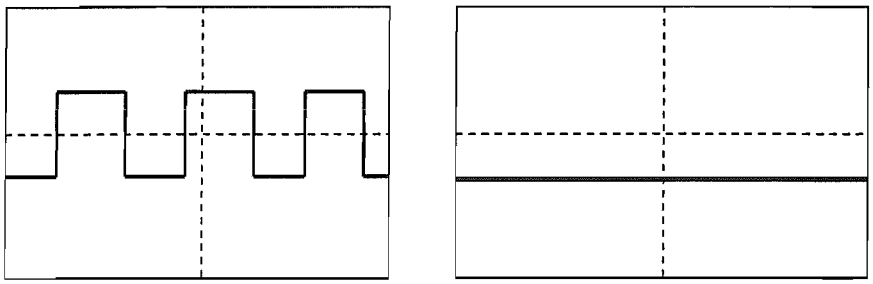

Figure 3.4. Oscilloscope screen with background noise (left) and compensated for noise (right).

3.4 References

1. "Exciton Spin Dynamics in Quantum Wells," T. Grevatt, PhD thesis, University of Southampton, (1996).

Page 28 missing

at each position the pump lens L1 was translated laterally across the slit of the photodiode in order to find the position that gave the strongest signal. Readings were made of the Vernier scale on L1 when the signal observed on the SR530 was one half maximum strength. This was done either side of the maximum and the difference between the two Vernier readings gave the spot size. (This is defined as the distance between the half maxima on each side of the centre of the spot.)This gave a pump spot size of 85 μm. the procedure was repeated for the probe beam giving a spot size of 70 μm.

4.2 Spatial Coincidence of the Beams.

In order to optimise the overlap of the pump and probe beams on the sample the following procedure was adopted. The laser was tuned to a wavelength expected to give a reasonable signal. The sample chamber in the cryostat was observed using a CCD camera linked to a monitor. This made it possible to judge the overlap of the beams by eye. The optical delay line was set to a point where a strong signal was expected, typically, ~16 ps. and the pump beam was translated laterally and vertically to maximise the difference signal. The signal is very sensitive to small changes in position of the pump lens.

As the sample and its holder expands and contracts as a function of temperature it is necessary to repeat this procedure each time the temperature in the sample space changes.

4.3 Temperature Measurement.

As this project involves temperature dependence of spin relaxation rate, it is necessary to contain the sample in a cryostat. At first a superconducting magnet cryostat (Oxford Instruments Cryomag) was used for time resolved and

photoluminescence measurements. Although limited data on magnetic field dependence was obtained, the cryostat was also used for all the temperature dependent measurements. The magnet cryostat contained a Variable Temperature Insert (VTI) in which a needle valve allows helium to enter the sample space in the centre of the cryostat. The temperature of this space is varied using a heater mounted in the sample chamber and controlled by an Oxford Instruments Intelligent Temperature Controller (ITC). A flow of gas through the cryostat is maintained by using a pump connected to the sample space.

For measurements not requiring a magnetic field the magnet cryostat was replaced with a Oxford Instruments continuous flow cryostat. This operated on the same principles as the VTI of the magnet cryostat except that instead of an internal helium bath the helium was supplied by a helium dewar linked to the cryostat by a siphon. The gas flow rate was varied by means of a needle valve on the siphon and a pump connected to the sample space.

A common problem with measurements performed in both cryostats was the necessity to be sure that the temperature on the face of the sample could be related to the temperature reading. Clearly the laser must produce some local heating effects so that the sample is at a higher temperature than that of the surrounding helium gas. Comparison of the results presented in chapter 7 with those obtained by the Shields group show that there seems to be a significant difference corresponding to perhaps a ~5K between the temperature shown on the ITC and the actual sample temperature.

4.4 Photoluminescence Measurements.

A helium-neon (HeNe) laser was used to create above barrier excitation of carriers. The electrons and holes then flow into the quantum well where they relax and recombine, emitting photons. This effect is known as photoluminescence (PL).

(See figure 3.1). The experimental set-up is shown in figure 4.2. For this project photoluminescence measurements on the sample were used for various characterisation purposes for example, determining the temperature dependence of the lowest energy transitions in quantum wells.

Page 32 missing

The helium neon laser is directed through an optical chopper, which provides the reference signal for the lock-in amplifier. The beam then strikes the mirror M1, which directs the beam onto mirror M2. The lens L1 focuses the light onto the face of the sample. A beam shield then stops the reflected beam. The emitted PL light is collimated by lens L2 and focussed onto a fibre optic cable by lens L3. A filter inserted between L3 and the fibre optic cable blocks light of wavelength >715 Å. This ensures that the signal is uncorrupted by laser light. The lens L4 focuses the light from the fibre optic onto the slit of a SPEX spectrometer. A stepper motor controller controls the position of the grating. This is moved in increments of (typically) 2 Å. The output slit of the spectrometer is connected to a photomultiplier tube whose output is sent to a lock-in amplifier. The output of the lock-in is sent to a PC data file.

A similar set up is used to measure the wavelength of the MIRA laser. This time a mirror is placed in the path of the pump beam, directing the light to the fibre optic cable. The spectrometer is then scanned until the peak of the signal is found.

4.5 Electroreflectance Measurements.

In order to locate the Fermi level in the two dimensional electron gas (2DEG) samples it is possible to use the photoluminescence excitation (PLE) spectrum. However an equally sensitive method which can be performed in the same geometry as the pump-probe time resolved measurements is the Electroreflectance measurement. PLE requires changing the sample orientation. Electroreflectance measurements involve adding an oscillating component to the usual bias applied to the gate on the sample (see figure 4.5 and the circuit diagram in figure 4.3) and observing the change in the reflected probe signal as a function of laser wavelength.

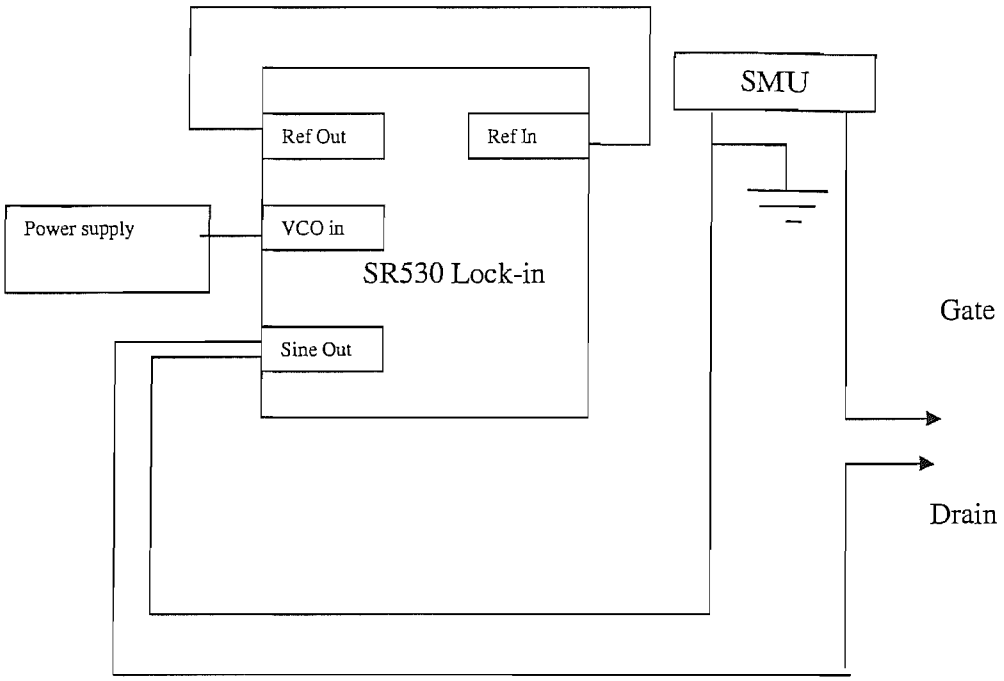

Figure 4.3 Electroreflectance set-up. The power supply drives the internal VCO of the lock in. This provides a 500Hz reference signal that is fed into the front panel reference circuit. The VCO also drives a sinusoidal signal of the same frequency and of bias 0.1V that is applied to the sample. The SMU provides an offset bias.

The pump beam is blocked and the chopper is stopped and the reference signal for lock-in detection is provided by the frequency of the applied oscillating voltage.

Figure 4.4 shows ER measurement compared with PL, PLE and pump-probe peaks for a typical case. It may be seen that the peak of the ER signal corresponds with the electron peak in the PLE and therefore the peak of the pump-probe signal.

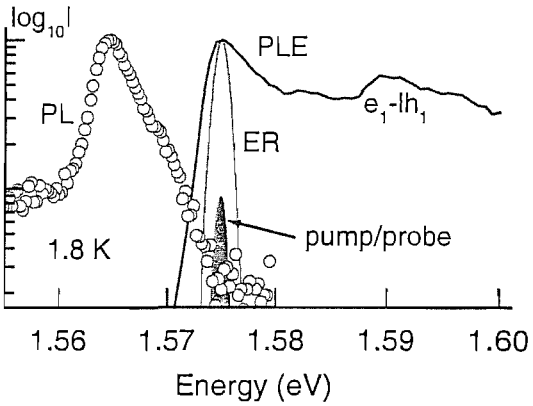

Figure 4.4. Energy profile of PL, PLE, ER and experimental pump probe signals. The time resolved measurements are taken at the top of the Fermi sea. Excerpted from Brand, (2003) [1].

This method unfortunately has its limitations. It is inefficient at higher temperatures because of smearing of the Fermi level due to thermalisation. However, at temperatures of less than or equal to 20K there is sufficient definition in the results to be able to pick out the Fermi level of the 2DEG and, as we shall see in chapter 7, excitonic effects.

4.6 Hall Effect Measurements.

Hall effect measurements were conducted to find the concentration and mobility of carriers in the 2DEG. The sample used in two of the three experiments in this work was processed into an FET structure with side contacts for Hall voltage measurements. (See figure 4.5 for a top down view of the sample.) The surface of the sample has a semitransparent metal layer for the Schottky gate. Varying the electrical potential of the gate changes the carrier concentration inside the well. The source, drain and Hall contacts are all electrically connected to the sample.

Hall measurements of the mobility and concentration were made using the arrangement shown in figure 4.5.

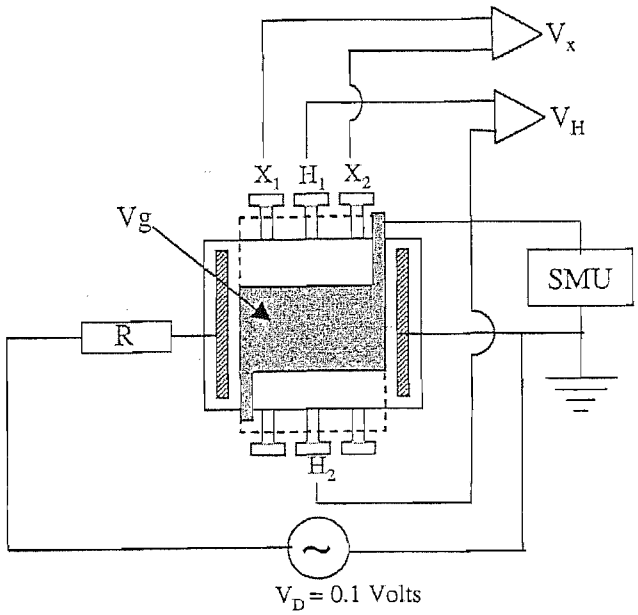

Figure 4.5. Set-up for measurement of concentration and mobility by the Hall effect. The potential between the gate and the channel was biased using a Source Measure Unit (SMU).

A small oscillating drive voltage was applied between the source and drain using the reference output from the digital lock in amplifier and a variable magnetic field was applied normal to the well. Measurements of the voltage drop across H_1 and H_2 and between X_1 and X_2 were used to determine mobility and concentration.

The mobility is related to the Hall and drive voltages by

$$\mu = V_h/(B_z V_x)$$

The concentration may be derived from

$$N = V_D B_Z/(ReV_H)$$

Where V_D is the drive voltage, R is the resistance in the circuit and e is the charge on the electron.

4.7 References.

1. "Optical time resolved spin dynamics in III-V semiconductor quantum wells," M. Brand, PhD thesis, University of Southampton, (2003).

CHAPTER 5

SPIN RELAXATION IN (110) ORIENTED QUANTUM WELLS.

5.1 Basic Theory

In section 2.3 it was mentioned that, as the pump and probe beams are perpendicular to the sample, when the angular moments of the photons are transferred to the electrons the electron spins are injected perpendicular to the plane of the well. The advantage of (110) oriented quantum wells is that the (110) axis lies perpendicular to the well's plane. Therefore the electrons have a much extended spin relaxation time. [1]

The long spin relaxation time for electrons in a (110) structure may be shortened by application of an electric field to the well. (This would be useful in creating a gateable spintronic device.) Returning to the equation for the D'yakonov Perel spin relaxation mechanism: [2]

$$\tau_s^{-1} = \langle\Omega^2\rangle\tau_p^* \qquad (2.1)$$

We have already discussed (in section 2.3) the spin splitting caused by the inversion asymmetry in the zinc-blende structure. This introduces a term to the spin precession vector known as the Bulk Inversion Asymmetry or Dresselhaus term, Ω_{BIA}. In the case of (110) oriented quantum wells, this lies in the growth direction of the well, perpendicular to the plane of the well. It does not contribute to relaxation of spins oriented along the growth direction, leading to greatly enhanced spin memory. The introduction of further asymmetry by altering the structure of the well (e.g., by asymmetrically varying the alloy composition in the barrier material on opposite sides of the well, or by a built in or applied bias) adds an extra component to the spin precession term $\langle\Omega^2\rangle$. This is known as the Structural Inversion Asymmetry or

Rashba term, (Ω_{SIA}.) The spin splitting arising from this term is known as the Rashba effect. [2, 3, 4] In perfect quantum wells symmetrical along the growth direction, this term will vanish resulting in Ω_{BIA} which may be switched by scattering but remains oriented along the growth axis. (See figure 5.1)

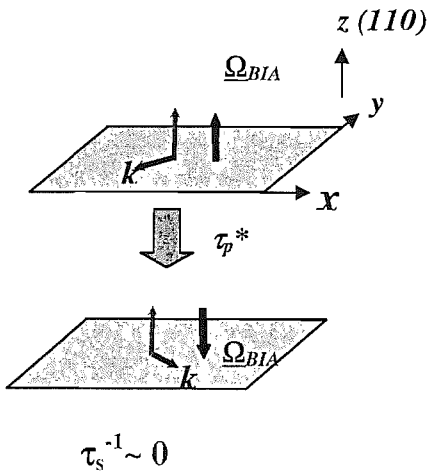

Figure 5.1. (110) quantum well with electric field $E_z = 0$. This leads to spin relaxation rates that tend to zero, as the BIA term does not cause spin precession. The crystal momentum lies in the plane of the well, as the movement of electrons is restricted in the z direction

However, an electric field applied perpendicular to the growth direction of the well (as is usually the case), or other asymmetry creates a spin precession vector Ω_{SIA} that lies in the plane of the well, at right angles to the bulk inversion asymmetry Ω_{BIA} and which fluctuates as a result of scattering (see figure 5.2).

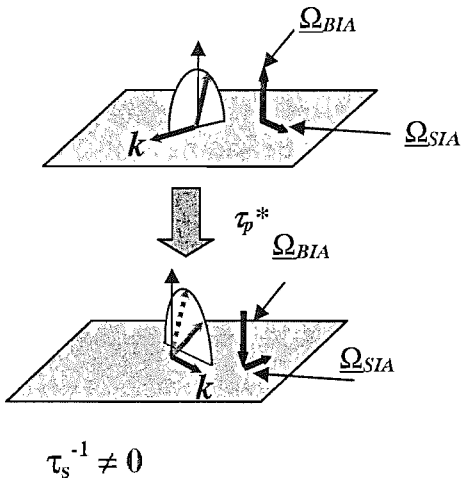

Figure 5.2. (110) quantum well with electric field $E_z \neq 0$. This introduces a structural inversion asymmetry term at right angles to the bulk inversion asymmetry contribution to the spin vector. The resultant spin precession vector acts upon the electron spin and causes it to precess. This leads to shorter spin relaxation times than in the $E_z = 0$ case.

Once this term is introduced, the resultant spin precession vector clearly lies at an angle to the growth direction and the electrons begin to precess in the fictitious internal magnetic field. Therefore, we may consider Ω_{SIA} as a field dependent term that contributes to spin relaxation along the growth axis. [5, 6]

This chapter will describe experimental investigation of predictions of this phenomenon, firstly by examining as-grown wafers for comparison of (110) and (100) orientations and secondly, a processed (110) p-i-n wafer with Au contacts attached to examine how the spin relaxation rate varies with applied electric field.

5.2 Sample Characteristics.

The samples used in these experiments were three multi-quantum well wafers each containing twenty 75Å quantum wells separated by 120Å barriers with aluminium fraction 0.4. The layers were deposited by molecular beam epitaxy by Dr

Mohamed Henini of Nottingham University. One of the wafers was grown on a (100) substrate and the other two were grown on (110) substrates. In order to test the contribution of Ω_{SIA} with varying bias one of the (110) oriented samples was grown as a p-i-n structure; (110) multiple quantum wells were grown between two 0.1 μm layers of undoped AlGaAs and with layers of $2*10^{18}$ cm^{-3} n^+ doped GaAs and of $1.2*10^{18}$ cm^{-3} p^+ AlGaAs respectively below and above. One of these samples was then processed into 400 μm diameter mesa structures as shown below in figure 5.3.

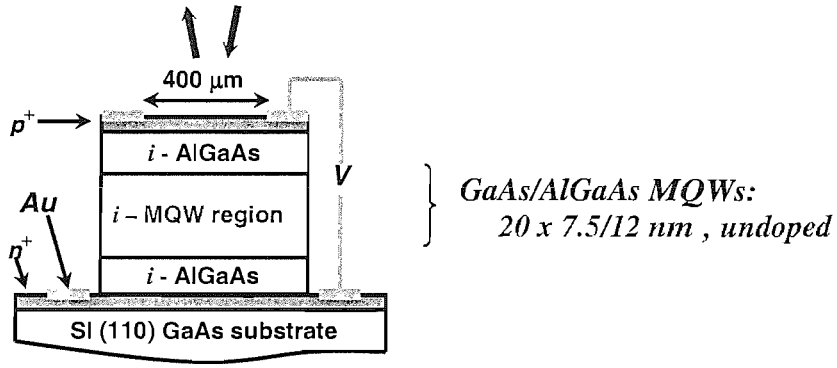

Figure 5.3. 400-μm cross-section GaAs/AlGaAs p-i-n mesa device showing incident and reflected beams for probing spin dynamics. The bias is applied through annular Au electrode deposited on the n^+ and p^+ layers.

Good epitaxial MBE growth on (110) substrates is difficult because As_4 does not stick easily to the non-polar (110) structure. In order to find the optimum conditions for MBE growth Dr Henini conducted several trial runs at creating (110) structures. Photoluminescence measurements to assess the quality of the interfaces are shown in figure 5.4.

In the first instance, a (110) wafer was grown under the same conditions as were optimum for a (100) wafer.

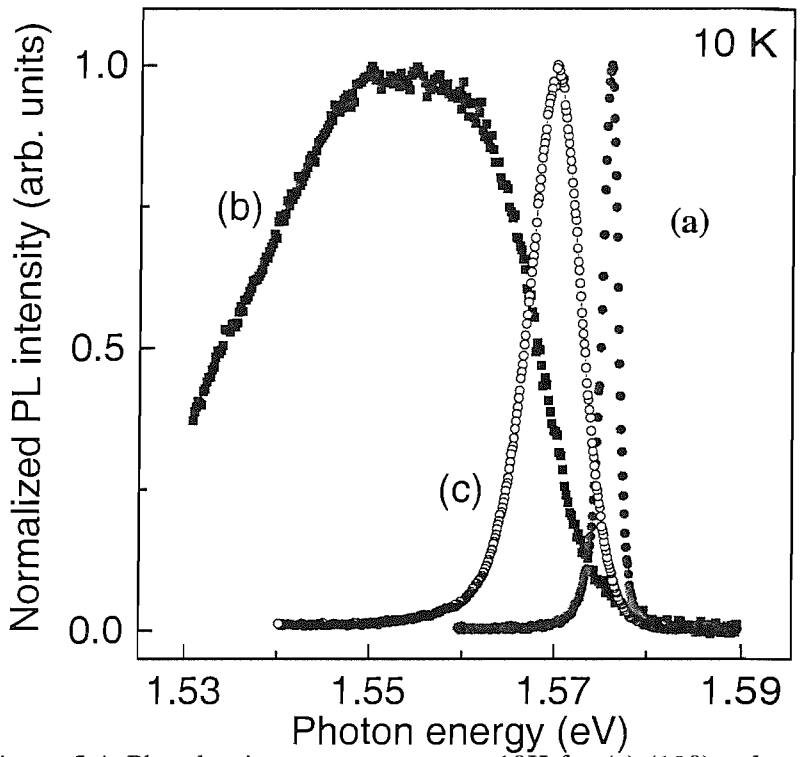

Figure 5.4. Photoluminescence spectra at 10K for (a) (100) substrate (b) & (c) (110) substrates. The MBE growth conditions for (a) and (b) were the standard ones for optimisation of (100)-oriented growth. The conditions for (c) were modified.

An early MQW structure grown on a (110) substrate (trace (b) in figure 5.4) did not produce a high quality well as is clear from the breadth of the PL feature. A second (110) wafer was grown, this time under different (lower) temperature and higher GaAs and AlAs flux conditions. This produced a well of much better quality (trace (c)), although still not as perfect as the (100) case under the same conditions (a). It can be seen that there is a pronounced difference between the PL line width for the (100) sample and that of the (110) sample. The width at 10K for the (110) sample is ~6.5 meV, but only 1.8 meV for the (100) sample. This suggests that the growth conditions for the (110) sample is less ideal than that of (100) growth. This leads to interface roughness and hence a less well-defined confinement energy. An estimate of this roughness may be made by comparing the width of the PL spectra.

The confinement energy, i.e., the difference between the band gap of GaAs and the energy of the peak of the PL is approximately proportional to the inverse square of the width of the well:

$$E_{conf} = E_{PL} - E_{gap}^{GaAs} \sim (L_z)^{-2}$$

Therefore, the interface roughness ΔL_z as a fraction of the well width L_z may be approximated as:

$$\Delta E/E \sim 2\Delta L_z/L_z.$$

For the sample of figure 5.4(c), $\Delta E/E \sim 6.5/50 \sim 0.13$ and hence $\Delta L_z/L_z$ has a value of 6.5%, or an interface roughness of the order of one monolayer. Further improvements in (110) growth are expected, and eventually it is hoped that (110) interfaces may be as smooth as that of (100) samples.

A PL measurement was also conducted on the (110) mesa device at 170K (see figure 5.5). The quantum well quality for this structure is very similar to that of the unprocessed structure shown in trace (c) in figure 5.4.

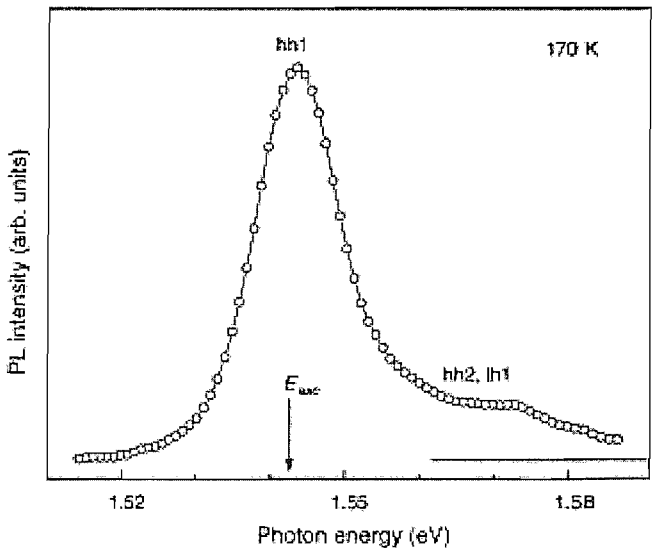

Figure 5.5. PL for (110) mesa structure taken at 170K.

The consequences of perfection of the interfaces for the time resolved results will be discussed in the next section.

5.3 Experimental Results

The first experiments conducted were time resolved measurements of the spin decay at 300K for the (100) wafer, the (110) wafer and the unprocessed (110) *pin* structure. These results are shown in figure 5.6.

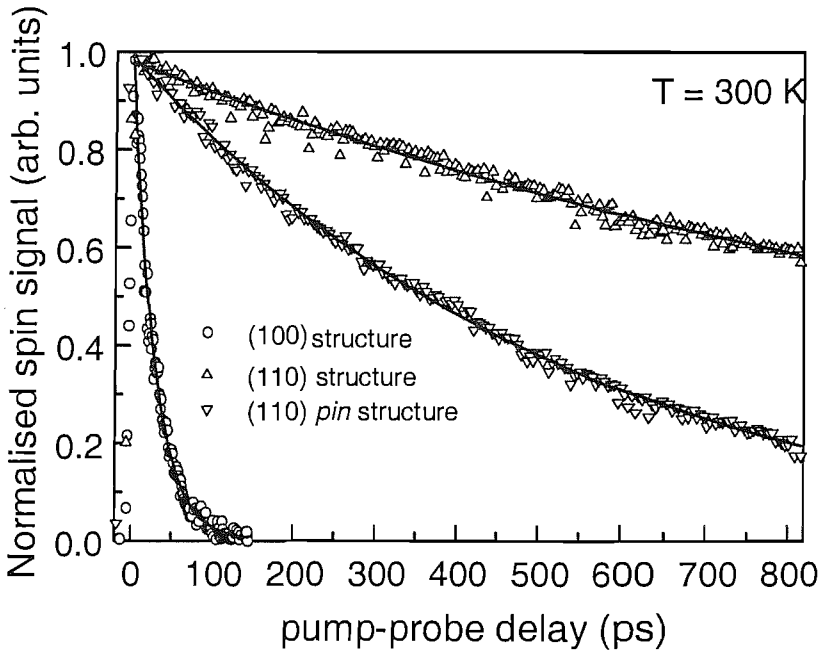

Figure 5.6. Spin decay measurements for (100), (110) and (110) *pin* multiple quantum well structures.

There is a dramatic increase in relaxation between the (100) wafer and the (110) wafer, showing that the DPK mechanism [4] is largely suppressed in the case of (110) structures. However, the decay for the pin structure, where there is a built-in electric field of 25 kV cm^{-1} at 300K, is significantly faster than for the undoped (110) MQW structure. The extracted spin relaxation times are, respectively, 32±1 ps for the (100) wafer, 3.5±0.2ns for the (110) wafer and 0.85±0.02 ns for the (110) pin wafer. These figures are consistent with the predictions described above as long as we

Page 45 missing

The dark current of the device shows very few carriers, but for the illumination used in the time resolved measurements there is increasing current for reverse bias greater than -1.5V. This strongly suggests avalanche multiplication.

It is very useful to compare this reverse bias current (which is of the order 0.8 μA) with the rate of photoexcitation of electron-hole pairs in the quantum wells under experimental conditions in order to verify that the current represents negligible sweep-out of the charge carriers during spin relaxation. We estimate the rate of absorption of photons in the N quantum wells of the i-region to be:

$R = P/(hc/\lambda)\ (1-\exp(-NL_z\,\alpha))$

Where P = incident laser power at the quantum wells,

λ = laser wavelength

L_z = quantum well width

α = absorption coefficient in the quantum wells m^{-1}

Assuming an incident power of 360 μW and making allowances for reflection at the sample surface and at the windows of the cryostat to the point where the expected photocurrent would be 30 μA if all the charge carriers were swept out of the wells. Therefore, less than 3% of the photoexcited carriers are lost in this way and the spin and population dynamics can be interpreted in terms of charge carriers confined in the wells during spin relaxation.

Figure 5.8 shows the spin decays for three time resolved runs at different values of applied voltage. These selected runs show that, under negative bias conditions, the spin relaxation follows a linear dependence on electric field.

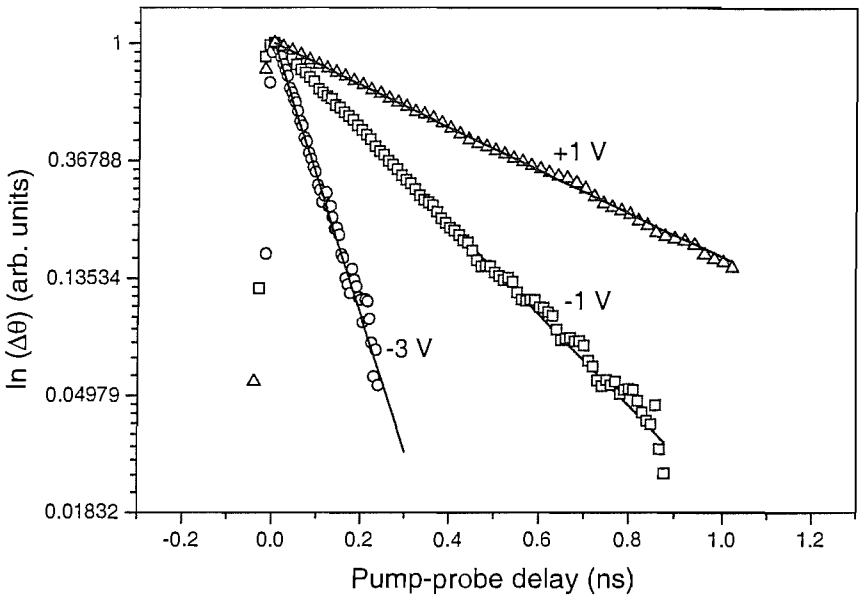

Figure 5.8. Spin decays for three applied voltages on the (110) mesa device. The spin relaxation becomes shorter with increasing bias.

Further runs were performed at a range of biases. The range of extracted values of spin relaxation rate as a function of electric field are shown in figure 5.9, compared with values calculated by Flatté and Lau [8] using a non-perturbative DPK approach for symmetrical quantum wells in applied electric field. The values for electric field are reliable because, although (as discussed below) the width of the wells may be non uniform, the overall width of the MQW structure is well known, as is the applied bias, so reliable measurements of kV cm^{-1} may be derived. The theory is scaled with an assumed mobility of 0.6 $m^2 V^{-1} s^{-1}$, the value expected based upon a room temperature value of 0.3 $m^2 V^{-1} s^{-1}$ and dominance of polar optic phonon scattering. The agreement of the two curves is very good for electric fields above 20 kV cm^{-1} but, at low fields (at, roughly, flat band conditions and below) there is clearly a contribution to spin relaxation not included in the calculations which presents a rate nearly 100 times lower than the observed values in zero field. The value assumed for the electron

mobility at room temperature has been confirmed experimentally by W. Leyland, Cavendish Laboratory Cambridge using the spin grating technique. [9]

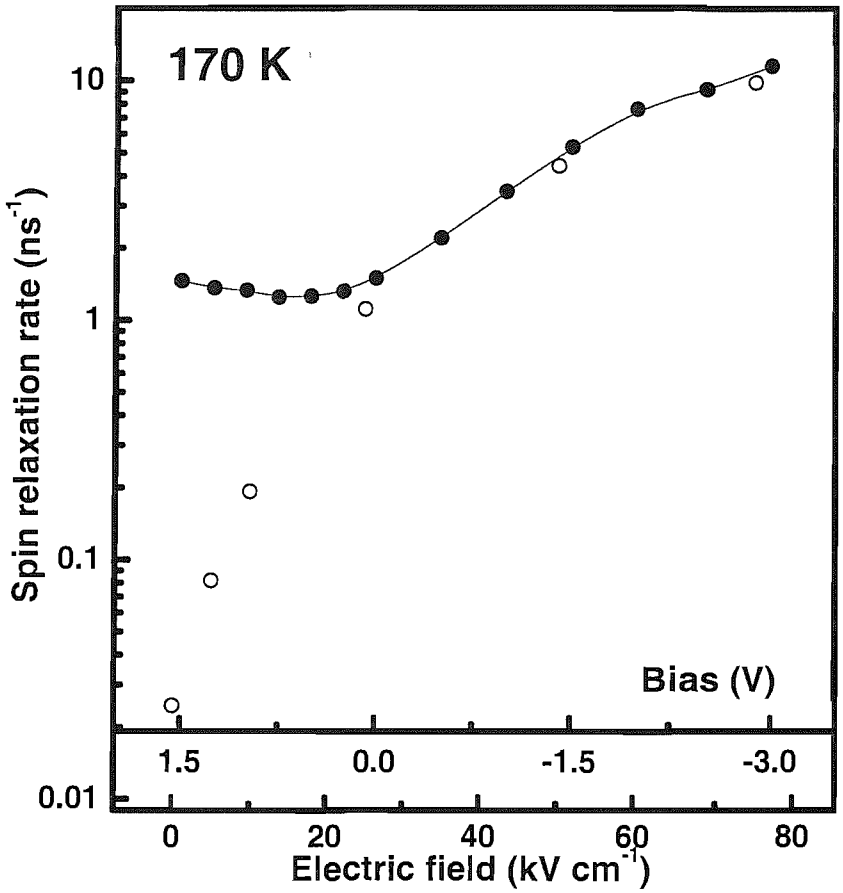

Figure 5.9. Extracted and calculated values for spin relaxation rate shown as a function of both gate voltage and electric field for electrons in the (110) oriented 7.5/20nm GaAs/AlGaAs quantum wells mesa device. The black circles represent the values extracted from experimental runs and the open circles represent the values derived from the calculations performed by Flatté and Lau. [8]

At first sight a possible explanation for this discrepancy may be the Bir-Aronov-Pikus (BAP) mechanism mentioned in section 2.3. This mechanism works by spin-flip interactions between the electrons and holes and gives a spin relaxation rate proportional to the hole concentration. The BAP mechanism may be more significant at low fields because a significant concentration of holes from the p-contact might then be injected or accumulate in the wells. Measurements of the recombination time

showed shorter values of τ_r at low fields, suggesting that at these fields electrons and holes are closer together and thus more likely to produce significant levels of BAP spin relaxation.

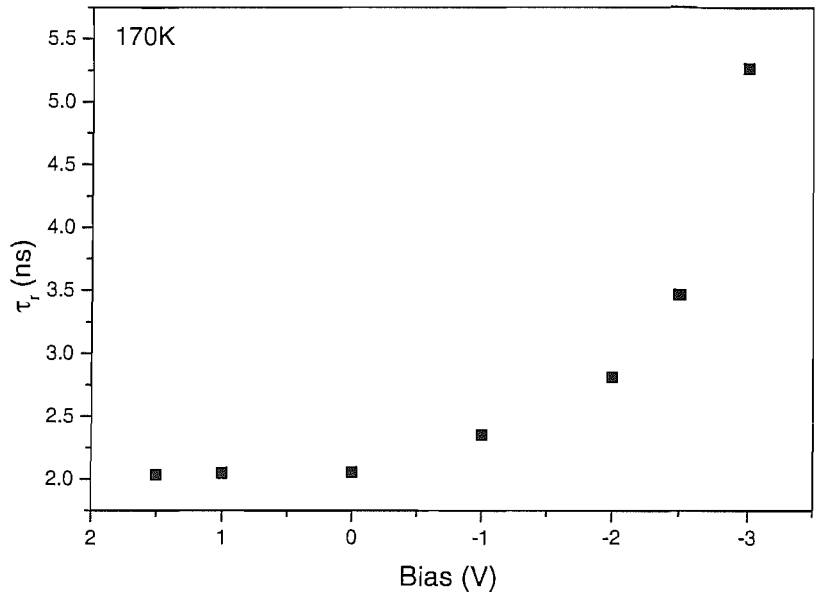

Figure 5.10. Recombination time of electron hole pairs in the (110) mesa device as a function of bias, showing increase of recombination time with applied field.

In order to ascertain the contribution of the BAP mechanism to the spin relaxation rate, it is therefore necessary to estimate the hole concentration in the wells at 170K and to calculate what BAP rate the concentration corresponds to. The maximum possible hole concentration due to photoexcitation is estimated to be $N_p = R\ \tau_r$ where R is the rate of photoproduction of electron hole pairs per unit area in the focused laser spot and τ_r is the recombination time.

$R = P/(hc/\lambda)(1-\exp(-NL_z\alpha).(\pi D^2)^{-1}$

D = diameter of spot (70 μm- see section 4.1 for a discussion of the method used to determine this.)

From the recombination data shown in figure 5.10, we can see that at low fields $\tau_r = 2$ ns. This gives a figure of $N_P \sim 2.8*10^{9}$ carriers (holes) m^{-2} per watt of pump power

(as $Np = R\tau_r$ and $P/(hc/\lambda) = 1.6$ electron hole pairs per second and $(1-\exp(-NL_z\alpha) = 0.14$, where $N = 20$, $L_z = 75$ nm and $\alpha = 10^6\ m^{-1}$)

The electrically injected hole density was estimated using a simulation program. These simulations indicated highly non-uniform distribution of holes for flat band bias conditions and a maximum concentration much lower than is required to cause levels of BAP spin relaxation high enough to account for the discrepancy shown in figure 5.9.

The BAP relaxation rate needed for a given concentration of holes may be estimated from two different sources. The graph for acceptor concentration versus relaxation rate quoted by Pikus and Titkov [12] gives values for hole lifetimes of $2.1 * 10^9\ s^{-1}$ for $N_A = 3.5 * 10^{17}\ cm^{-3}$ and $1.3 * 10^9\ s^{-1}$ for $N_A = 2.2 * 10^{17}\ cm^{-3}$, indicating a rate of order $6.0 * 10^{-9}\ s^{-1}\ cm^{-3}$, and secondly, the values calculated by Lampel and Fishman [13] which give a result of $12.5* 10^{-9}\ s^{-1}\ cm^3$. Dividing by the width of the twenty wells, (150 nm) this gives a value per unit area of $0.8\ s^{-1}\ cm^{-2}$. The maximum value for the BAP relaxation rate is therefore:

$$\tau_{BAP}^{-1} = 2.8*10^9 *0.08\ s^{-1}$$

$$= 0.24\ 10^9\ s^{-1}$$

The observed rate is about $1.2 * 10^9\ s^{-1}$. (See figure 5.9)

Therefore, we conclude that the BAP relaxation only makes a small contribution to the large discrepancy between experimental and calculated values. It is obvious that we must look elsewhere for an explanation.

As a second possibility it was considered that the origin of the extra spin relaxation might be random built in asymmetry due to the interface roughness (which can be deduced from the width of the PL, see previous section). This asymmetry could result from alloy fluctuations or from differences of top and bottom interface

morphology for the GaAs quantum wells. This would generate a field independent Ω_{SIA} term that would vary from point to point along the quantum well with associated non-zero mean square precession frequency. As seen above, the PL spectra for the (110) quantum wells show that the growth quality is significantly worse than the (100) case and that the line width suggests random asymmetry approximately equivalent to one or two monolayers. Flatté and Lau [8] performed further calculations in an attempt to simulate the effect of such asymmetry. The simulation presumed a quantum well with one perfect interface and one with a one monolayer compositional gradient in zero electric field. This compositional gradient is described by a layer of $Al_{0.2}Ga_{0.8}As$ extending one monolayer on either side of the normal interface location. The calculation of this effective $Al_{0.2}Ga_{0.8}As/GaAs$ quantum well gives a relaxation rate ~30 times greater than that of the initial zero field calculated value. Even this small perturbation of the symmetry produces a change approaching our discrepancy between theory and experiment. This supports the notion that the discrepancy between experiment and calculation can be largely ascribed to built in asymmetry due to less than perfect growth conditions.

In conclusion, enhanced high-temperature electron spin memory in (110) quantum wells may be varied by up to a factor of 10 by application of bias voltages. This variation is consistent with the Rashba effect and the DPK [4] spin relaxation mechanism. However, growth conditions of the well significantly affect the spin relaxation indicating that further improvement in the growth process may lead to a useful improvement in the gateability of the spin relaxation.

5.4 Variation of the Spin Relaxation Rate with Magnetic Field.

Further measurements on the (110) unprocessed *pin* wafer were conducted in order to investigate a possible method suggested by Ivchenko [11] for separating the contribution of the mean square precession frequency from the momentum scattering time in the equation (see section 2.1 [2]) for the spin relaxation rate due to the DP mechanism [3]. For this to be done a magnetic field is applied to the sample in the growth direction of the well. This is expected to give the following for the magnetic field dependence of the spin relaxation rate:

$$\tau_s(B)^{-1} = \tau_s(0)^{-1}/(1 + (\omega_c\tau_p^*)^2)$$

where ω_c = cyclotron frequency = eB/m_e^* (where m_e^* = effective mass.) [11]

For the purposes of this chapter, it is reasonable to assume that $\tau_p^* \approx \tau_p$. This is a valid assumption as the wells in the sample under investigation are not modulation doped so electron-electron scattering does not make a significant contribution to the spin relaxation. Clearly direct measurement of the transport relaxation time is difficult for intrinsic wells and a method of separating the terms in the DP formula [3] is desirable. Similarly, where direct transport measurements are possible electron-electron scattering can come to dominate the spin dynamics (see the following chapter) and again a method for separating the terms is desirable.

An external magnetic field **B** causes precession of electron momentum $\hbar\mathbf{k}$ about the field direction, with the cyclotron frequency ω_c. In a high magnetic field, where $\omega_c\tau_p^* \gg 1$, the average values of momentum components perpendicular to the direction of **B** reduce to zero and only the momentum component parallel to the direction of **B** does not vary. Averaging all components of the vector over all **k**

directions $\mathbf{k} \perp \mathbf{B}$ leads to zero values, which means a complete suppression of the DP mechanism, so that other mechanisms determine the spin relaxation.

The dependence of spin relaxation rate upon external magnetic field shows a Lorentzian curve. It may be seen from the above equation that when $\tau_s(B)^{-1} = \frac{1}{2}\tau_s(0)^{-1}$ then $(\omega_c\tau_p^*) = 1$. As the cyclotron frequency is already known it should be possible to calculate the mean square precession frequency. However, bearing in mind the presence of other spin relaxation mechanisms besides the DPK which are either not affected by the magnetic field, or are affected in different ways, it is possible that the spin relaxation rate does not decrease to zero with a large magnetic field. For a valid analysis, it is necessary to adjust the above equation in order to reflect this:

$$\tau_{s(B)}^{-1} = \tau_{s(0)}^{-1}/(1 + (\omega_c\tau_p^*)^2) + \tau_{s(\infty)}^{-1}$$

where $\tau_{s(\infty)}^{-1}$ is the offset, non-magnetic field dependent part of the spin relaxation.

5.4.1 Experimental Set-up.

The apparatus was set-up in the standard pump probe geometry, with the magnet cryostat described in section 4.3.

5.4.2 Experimental Results.

The excitation power and wavelength of the laser were kept constant while the magnetic field was decreased by increments of 0.5 T from a maximum of 3 T. The results are shown in figures 5.11, 5.12 and 5.13.

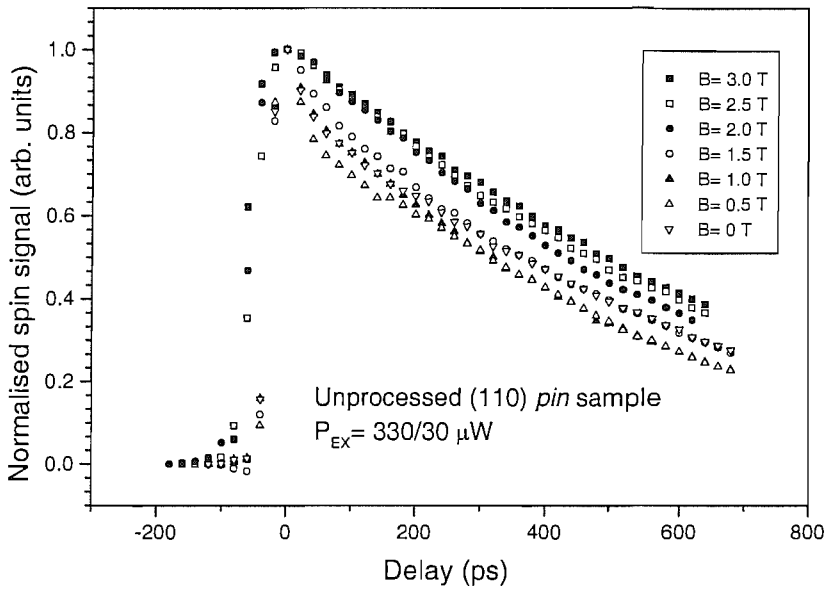

Figure 5.11. Spin decay as a function of magnetic field for an unprocessed (110) *pin* sample. The extracted values of spin relaxation rate are shown in figure 5.12

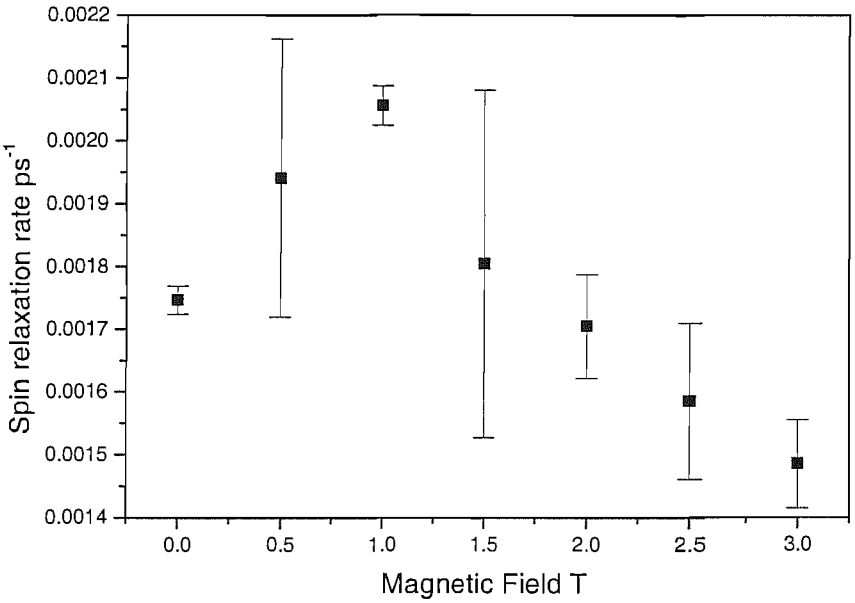

Figure 5.12. Spin relaxation rate as a functional of longitudinal external magnetic field for an unprocessed (110) wafer. Derived from the data shown in figure 5.11 above.

At low fields the data shown in figure 5.12 seems to show an increase in the spin relaxation rate with increasing field. At high fields, the rate increases in apparent accordance with the predictions of the Ivchenko [11] theory. However, this trend is not repeated in the data shown in figure 5.13.

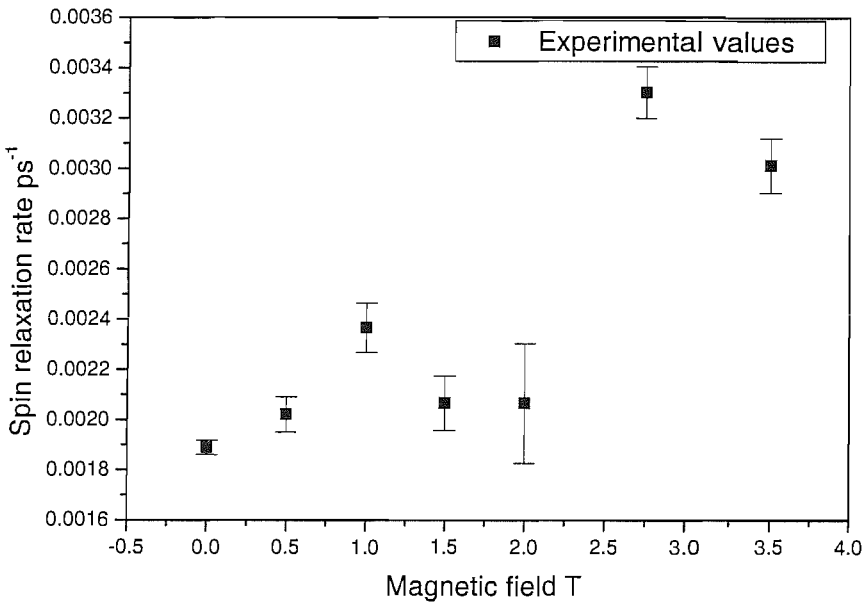

Figure 5.13. Second set of extracted values of spin relaxation rate as a function of longitudinal magnetic field for an unprocessed (110) wafer.

The irreproducibility of the results is due to some unknown factor and further study is required to get the method to work reliably. It may be significant that spin relaxation times in (110) quantum wells are so long that any change of spin relaxation time could be difficult to detect due to the extremely long runs needed to observe the slight changes in spin decay caused by the magnetic field. The length of runs is limited by the length of the delay line and the time before the helium cooling the magnet runs out. In future it may be better practice to perform magnetic field dependence measurements on (100) samples, which have short relaxation times that

make changes due to applied magnetic field easier to detect and should help to establish the method for separation of the terms in equation 2.1. It might be argued that the failure to observe the expected field dependence of the spin relaxation rate indicates an absence of the DPK mechanism in the (110) samples. However, it is clear that DPK spin relaxation is still present. The observed spin relaxation times are too short to be accounted by the Elliott-Yafet spin relaxation mechanism and BAP relaxation has been ruled out in the previous section. Additionally, our measurements on (110) samples in zero field agree closely with the calculations of Flatté and Lau based on DPK spin relaxation. [8]

5.5 Conclusion.

The work presented in this chapter has demonstrated that the enhanced high-temperature electron spin memory in (110)-oriented quantum wells may be varied by at least a factor of 10 by application of modest bias gate voltages. This variation is consistent with the Rashba effect and the DPK spin relaxation mechanism. On the basis of this mechanism, the measurements for low electric fields indicate that a further significant enhancement of spin memory may be achieved by modification of the growth techniques to optimise the interface morphology. This can lead at 300K simultaneously to high electron mobility; spin memory of order 10 ns and straightforward voltage bias control. This combination of properties may be expected to facilitate a variety of room temperature spintronic devices.

Although attractive as a tool for separating terms in the DPK relaxation formula, Ivchenko's predictions of the magnetic field dependence of the DPK mechanism are not yet borne out experimentally. More work needs to be done in this area, including (100) quantum well samples where the zero-field relaxation rate is greater.

5.6 References.

1. "Spin relaxation in GaAs (110) quantum wells," Y. Ohno, R. Terauchi, T. Adachi, F. Matsukura and H. Ohno. Phys. Rev. Lett., **83** 4196, (1999).
2. "Spin-orbit coupling effects in zincblende structures," G. Dresselhaus, Phys. Rev. **100** 580 (1955).
3. "Spin relaxation of conduction electrons in noncentrosymmetric semiconductors," M. I. D'yakonov and V. I. Perel, Sov. Phys. JETP **33** 1053 (1971).
4. "Spin relaxation of two-dimensional electrons in noncentrosymmetric semiconductors," M. I. D'yakonov and V. Yu. Kachorovskii, Sov. Phys. Semicond. **20** 110 (1986).
5. "Precession spin relaxation mechanism caused by frequent electron-electron collisions," M. Glazov and E. L. Ivchenko, JETP Letters, **75** 403.
6. "D'yakonov-Perel spin relaxation under electron-electron collisions in n-type QWs," M. Glazov, E. L. Ivchenko, M. A. Brand, O. Z. Karimov and R. T. Harley, Proceedings of the international symposium "Nanostructures: Physics and Technology", St.-Petersburg, Russia (2003).
7. "Gated spin relaxation in (110) quantum wells." Henini, M., Karimov, O.Z., John, G.H., Harley, R.T., Airey, R Physica E **23** 309-314 (2004).
8. "High temperature gate control of quantum well spin memory." Karimov, O.Z., John, G.H., Harley, R.T., Lau, W.H., Flatte, M.E., Henini, M., Airey, R. PRL **91**, 246001 (2003).
9. "Four wave mixing studies of diffusion and spin relaxation in semiconductor quantum wells," W. Leyland, Transfer report, Clare College Cambridge, (2004).

10. "Tunability of electron spin coherence in III-V quantum wells." W. H. Lau and M. E. Flatté, J. Appl. Phys. **91** 8682 (2002)
11. "Spin relaxation of free carriers in a noncentrosymmetric semiconductor in a longitudinal magnetic field." E.L. Ivchenko, Sov. Phys. Solid State, **15** 1048.
12. "Optical Orientation," edited by F. Meier and B.P. Zakharchenya, North-Holland, Amsterdam (1984).
13. "Spin relaxation of photoelectrons in p-type gallium arsenide". G. Lampel and G. Fishman, Phys Rev B, **16** 820 (1977)

CHAPTER 6

TEMPERATURE DEPENDENCE OF SPIN RELAXATION RATE IN A MODULATION DOPED QUANTUM WELL.

This chapter describes measurements of the electron spin relaxation time taken at temperatures between 10K and 275K in a high quality modulation doped quantum well. The transport and momentum relaxation times and the mean square precession frequency of electrons in the two dimensional electron gas (2DEG) were extracted from the experimental data and their temperature dependences were compared with the theoretical predictions.

6.1 Theoretical Background.

The D'yakonov-Perel formula for representing spin relaxation was shown in section 2.3. [1]

$$\tau_s^{-1} = \langle\Omega^2\rangle\tau_p^* \tag{6.1}$$

It was previously shown that the assumption that τ_p^* (the momentum relaxation time) is identical to τ_p (the transport relaxation time, from which the mobility is derived by $\mu = e\,\tau_p/m_e^*$) is not correct in all cases, as it fails to take into account the contribution of electron- electron scattering. This becomes significant in a modulation doped quantum well [2] It is useful to rewrite the above expression as:

$$\tau_s^{-1} = \langle\Omega^2\rangle(\tau_p^{-1}+\tau_{ee}^{-1})^{-1} \tag{6.2}$$

where τ_{ee}^{-1} is the electron-electron scattering rate.

The following sections will examine the temperature dependence of τ_p^{-1}, τ_{ee}^{-1} and $\langle\Omega^2\rangle$ and hence the predicted temperature dependence of τ_s^{-1}.

6.1.1 Scattering mechanisms.

6.1.1.1 The transport relaxation time τ_p as a function of temperature

The three scattering processes that may be expected to contribute to the transport relaxation time are thermal vibrations, scattering from ionized impurities and scattering from neutral impurities. In each of these cases the scattering time τ will be a function of the energy E and we require an average of the energy over the electron energy spectrum. The value of a function of the form E^j, when averaged over a Maxwellian energy distribution is of the order $(k_BT)^j$. Therefore if τ is a function of the form constant*E^j then:

$$<\tau(E)> = \text{constant}^* E^j \approx \text{constant}^*(k_BT)^j \text{ [3]} \qquad (6.3)$$

6.1.1.1.1 Scattering by thermal vibrations.

In the case of scattering of electrons due to thermal vibrations, electrons will only be scattered to nearby vacant states, as the phonon energy is very much lower than the electron energy. The scattering probability depends upon the number of vacant states that the electron may be scattered into. This probability is proportional to the total density of states ρ. For electrons in bulk material this is proportional to the square root of the energy. The scattering also depends upon the square of the amplitude (i.e., the energy) of the thermal vibrations. The thermal vibrations term of the transport relaxation time is therefore:

$$\tau_{g(E)} = \text{constant}^*(k_BTE^{1/2})^{-1} \qquad (6.4)$$

and the average over all possible states:

$$<\tau_{g(E)}> = \text{constant}^*(k_BT)^{-3/2} \qquad (6.5)$$

Therefore, the thermal vibration scattering term of τ_p has a temperature dependence of $T^{3/2}$. The contribution to τ_p^{-1} from τ_g^{-1} increases as the temperature is increased. [3]

However, in a two dimensional system, the density of states is constant independent of energy, and this means that the thermal scattering is governed only by k_BT. Therefore the temperature dependence is T^1. It is also important to bear in mind the increased contribution from optical phonon scattering at high temperatures in 2D structures. When this effect becomes pronounced the temperature dependence tends to T^2. [4]

6.1.1.1.2 Scattering by ionized impurities.

Scattering by ionized impurities may be analysed by applying the Rutherford formula for small angle scattering. This gives a scattering cross section that is proportional to $e^4(\Delta Z^2)/E^2$, where e is the charge on an electron, ΔZ the effective charge on an ion and E is the energy of an incident electron. When applied to non-metals this expression must take into account the dielectric constant ε. This reduces the interaction by ε^2. The mean free path is then:

$$l = \text{constant}*\varepsilon^2 E^2/\{ e^4(\Delta Z^2)\} \qquad (6.6)$$

As the velocity is equal to $(2E/m_e^*)^{1/2}$, the transport relaxation time for electrons scattered by ionized impurities may be written as:

$$\tau_i = lN_i/v = \text{constant}*N_i m_e^{*1/2}*\varepsilon^2 E^{3/2}/\{ e^4(\Delta Z^2)\} \qquad (6.7)$$

Again, taking the average over all possible states:

$$<\tau_{i(E)}>= \text{constant}* N_i m_e^{*1/2}*\varepsilon^2 (k_BT)^{3/2}/\{ e^4(\Delta Z^2)\} \qquad (6.8)$$

where N_i = ionised impurity concentration

Hence, it can be seen that the temperature dependence is the inverse of the thermal vibration case, and therefore τ_i becomes the dominant mechanism as the temperature is reduced. [3]

The above fails to take into account the special circumstances of a modulation doped quantum well. In a two dimensional system, the effect of the impurities on the

scattering is profoundly different. This is because the structure is doped only in the barrier material, while the well itself is of high purity. This means that the contribution of the dopants to the scattering is very much reduced. The difference between the mobilities as a function of temperature in bulk and modulation doped quantum well GaAs is shown in figure 6.1. [4]. Since the mobility is directly proportional to scattering time this illustrates the temperature dependences of the transport relaxation time in th two cases.

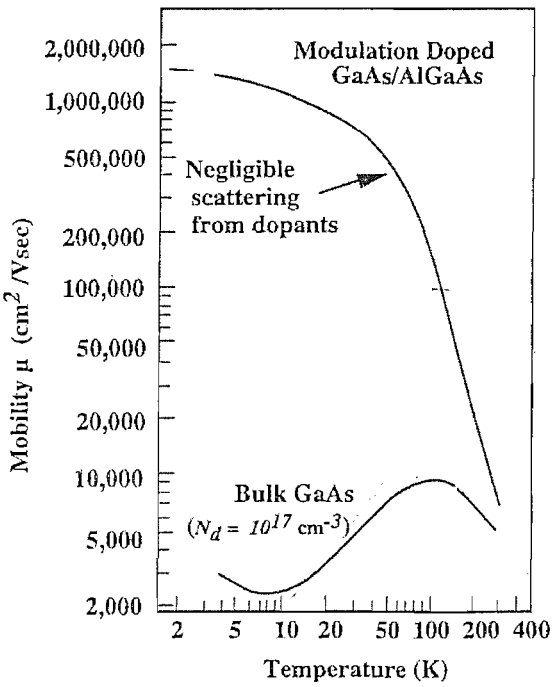

Figure 6.1. Typical mobility versus temperature for a modulation doped and uniformly doped (bulk) GaAs structures. The mobility for the modulation doped structure is larger as the absence of impurities means there are fewer scattering events. Excerpted from Weisbuch and Vintner. [4]

The mobilities for bulk and QW cases only approach each other at higher temperatures when thermal vibration scattering becomes significant (see figure 6.2. for a log-log plot.)

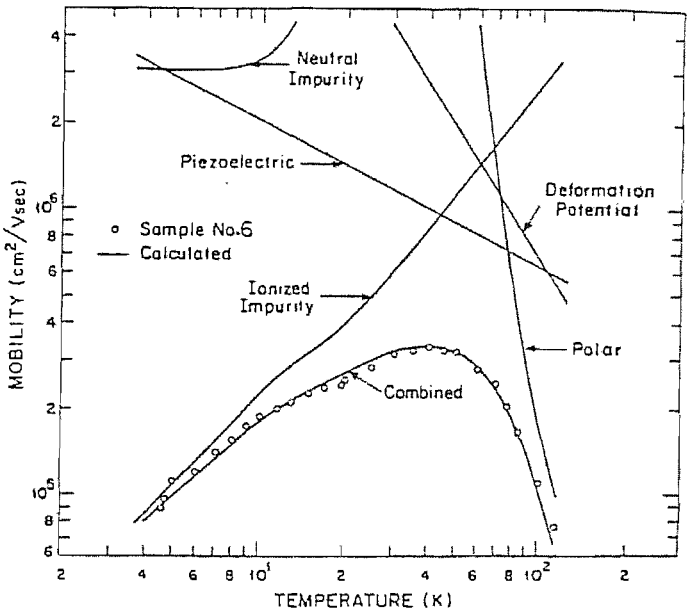

Figure 6.2. Log-log plot of mobility versus temperature for a bulk GaAs sample. The circles show experimental values of mobility. The polar optic scattering line shows the bulk value of thermal scattering approaching the quantum well case. Excerpted from Weisbuch and Vintner. [4]

The transport relaxation rate for the AlGaAs/GaAs quantum well is therefore the sum of the two rates considered:

$$\tau_p^{-1} = \tau_i^{-1} + \tau_g^{-1} \qquad (6.9)$$

6.1.2 Degeneracy.

Before the temperature dependences of the mean square precession frequency and the electron-electron scattering rate are discussed, it is necessary to outline the concept of degeneracy. This is important because the mean square precession frequency and the electron-electron scattering rate behave differently depending on whether the electrons are in a degenerate or non-degenerate state.

In a doped semiconductor with a large number of impurities the assumption that the system always follows Maxwell-Boltzmann statistics is not longer valid. This

is because the number of carriers created is no longer small compared with the number of vacant states in the conduction band that they may occupy. At low temperatures the electrons will only be excited to states at the bottom of the conduction band where the density of states is small. (This assumption does not hold for quantum wells- see further discussion below.) Therefore, the Pauli Exclusion Principle applies and the Fermi-Dirac statistics are needed to describe the system, i.e., the electrons behave as though they are in a metal or semi-metal. Here, the electronic Fermi sea is degenerate and the Fermi level lies in the conduction band rather than in the band gap. If the Fermi level E_F (measured from the bottom of the conduction band) is very much larger than k_BT then all the low lying states below the Fermi level will be filled, just as in a metal. As the temperature is increased, the Fermi distribution changes from a step function and its edge becomes smeared. (See figure 6.4)

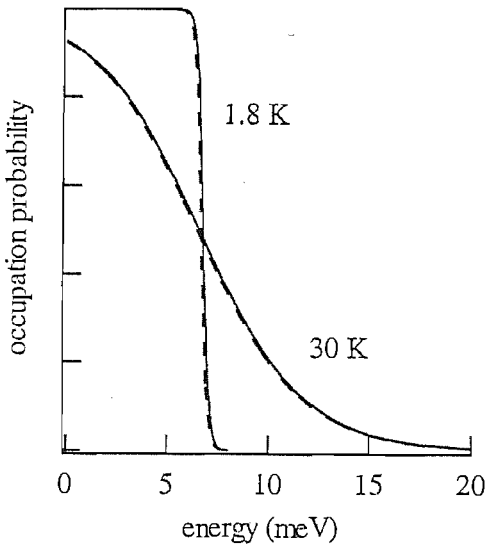

Figure 6.4. Occupation probabilities for conduction band electrons at 1.8K and 30K in a 2DEG containing approximately1.8 $*10^{11}$ electrons per square centimetres. The dotted and continuous lines represent left and right circular polarisations of pump light. Excerpted from Brand [8].

Once this smearing becomes of the order of ~ k_BT, the number of available states increases to the point at which the Fermi-Dirac statistics are no longer distinguishable from Maxwell Boltzmann statistics and the system passes from a degenerate to a non degenerate state. It is possible to define a Fermi temperature T_F at which this transition happens:

$$E_F = k_B T_F \tag{6.10}$$

In the case of bulk semiconductors:

$$T_F \approx \text{constant}.n_e^{2/3} \tag{6.11}$$

Where n_e = concentration of electrons.[4]

The quantum well case differs because the density of states has a different dependence on energy. In bulk semiconductors the DOS increases as the energy is increased. In a 2D system the density of states is constant, independent of energy.

$$\rho_{2D} = m_e^*/(\pi\hbar^2) \tag{6.12}$$

$$E_F = N_s\ (\pi \hbar^2\ )/(\ m_e^*) \tag{6.13}$$

where N_s is the electron concentration per unit area. Therefore, in a quantum well the Fermi temperature depends linearly upon the electron concentration. In the work under discussion T_F is ~70K but the position of the minima in the graph of spin relaxation rate versus temperature may vary as a function of concentration.

6.1.3 The mean square precession frequency as a function of temperature.

6.1.3.1 The mean square precession frequency in the degenerate case

As we have seen in section 2.3, in the three-dimensional case the spin splitting in the conduction band follows the rule $\Omega \sim k^3$. [1] In the 2D case, the quantization of the crystal momentum in the z direction alters this spin splitting [5, 6]

$$\Omega \sim (k_z + k_\perp)^3 \tag{6.14}$$

Multiplying out this gives:

$$\Omega \sim k_z^3 + 3\,k_z^2\,k_\perp + 3\,k_z\,k_\perp^2 + k_\perp^3$$

and hence to a first approximation, replacing k_z by its expectation value:

$$\Omega_{(k\perp)} \sim \langle k_z \rangle^3 + \langle k_z^2 \rangle k_\perp + \langle k_z \rangle k_\perp^2 + k_\perp^3 \qquad (6.15)$$

Of these four terms, $\langle k_z^3 \rangle$is equal to zero, and the last two terms are small enough to be negligible as $\langle k_z^2 \rangle >> k_\perp^2$. The only term that gives an appreciable contribution to Ω is $\langle k_z^2 \rangle k_\perp$. As k_z represents quantization in the z direction it may be correlated with the confinement energy E_{1e}. As $k_\perp$ corresponds with motion in the xy plane it corresponds to E_F. Thus:

$$\langle \Omega^2 \rangle \sim E_{1e}^2 E_F \qquad (6.16)$$

This may be approximated to:

$$\langle \Omega^2 \rangle \sim E_{1e}^2 N_s \qquad (6.17)$$

as the Fermi level is determined by the electron concentration N_s. This shows that the mean square precession frequency is directly proportional to the electron concentration when the electron system is in a degenerate state.

6.1.3.2 The mean square precession frequency in the non-degenerate case.

When $T>T_F$, the electron system is non-degenerate, and the Boltzmann distribution applies. Therefore, as k_BT is now larger than E_F, we may rewrite expression 6.16 as:

$$\langle \Omega^2 \rangle \sim E_{1e}^2\, k_B T \qquad (6.18)$$

In the non-degenerate system the mean square precession frequency is directly proportional to temperature and independent of electron concentration.

6.1.4 The electron-electron scattering rate as a function of temperature.

6.1.4.1 The electron-electron scattering rate in the degenerate case.

To consider the contribution of the electron-electron scattering, consider the following expression derived by Zheng and Das Sarma[7] for the scattering rate at energy E_F in a 2DEG:

$$\tau_{ee}^{-1} \sim ((\pi E_F)/(4\hbar))(kT/E_F)^2 \ln(kT/E_F) \qquad (6.19)$$

Therefore for electrons injected at the Fermi energy we expect (neglecting the logarithmic term :)

$$\tau_{ee}^{-1} \sim E_F^{-1} T^2 \qquad (6.20)$$

As the Fermi level is determined by the electron concentration, this may be rendered as:

$$\tau_{ee}^{-1} \sim N_s^{-1} T^2 \qquad (6.21)$$

This formula shows a scattering rate inversely proportional to electron concentration. This is a peculiar feature of a degenerate electron gas. For a fully degenerate electron gas the scattering rate at the Fermi energy vanishes due to the Pauli principle as may be seen by setting T=0 in equation 6.19. As the electron concentration is increased at constant temperature the electron gas becomes more degenerate and consequently the electron-electron scattering rate is reduced.

6.1.4.2 The electron-electron scattering rate in the non-degenerate case.

When $T>T_F$, the electron system is non-degenerate and according to Esipov and Levinson [10]:

$$\tau_{ee}^{-1} \sim N_s T^{-1} \qquad (6.22)$$

This function shows the intuitively expected linear dependence of scattering rate on electron concentration and an inverse temperature dependence that reflects the inverse energy dependence of the Coulomb scattering of classical charged particles.

6.1.5 Summary.

The different components for each case, degenerate and non-degenerate, may be summarised to two general equations:

$$\tau_s \sim (N_s^2 E_{le}^2)^{-1} (A + B(T^2)/N_s) \text{ for the degenerate case;} \quad (6.23)$$

$$\tau_s \sim (TE_{le}^2)^{-1}(CT^2 + (D N_s/T)) \text{ for the non-degenerate case.} \quad (6.24)$$

Where A, B, C and D are constants representing, respectively, impurity scattering, electron-electron scattering in the degenerate regime, phonon scattering and electron-electron scattering in the non-degenerate regime.

The work in this chapter will investigate the predicted temperature dependence for a 2DEG in a 10nm quantum well. It may be seen that the effect of electron-electron scattering is expected to show a striking peak in the spin relaxation time at a temperature of order T_F. At low T the variation is T^2 and at high T it is T^{-2}.

6.2 Experimental Method.

The experiments were conducted on a 10 nm $Al_{0.33}Ga_{0.67}As$/GaAs quantum well sample grown by Professor D. Ritchie, Cavendish Laboratory, Cambridge, and processed by D. Sanvitto, Toshiba, Cambridge. The layer structure of this sample consisted of 1μm semi-insulating (100) GaAs substrate, 1μm $Al_{0.33}Ga_{0.67}As$, 0.5μm GaAs(25A)/ $Al_{0.33}Ga_{0.67}As$(25A) superlattice, 100 Å quantum well, 600 Å undoped $Al_{0.33}Ga_{0.67}As$ spacer, 2000 Å $Al_{0.33}Ga_{0.67}As$(Si doped 10^{17} cm^{-1}) and a 170 Å GaAs cap. The sample was processed into a field effect transistor with a semi-transparent Schottky gate contact and Ohmic contacts to the quantum well. (See figure 6.1.) The

application of a bias between the gate and Ohmic contacts allowed the electron concentration in the well to be varied. For this type of structure the electron concentration tends to be a maximum at zero bias and is set by the modulation doping and layer thickness. Application of negative bias to the gate then depletes the quantum well. For this particular sample it was found that a small positive bias was required to saturate the electron concentration in the well. The bias was applied by using a source measure unit (SMU). The maximum current the SMU could supply was set at 1μA. This was to ensure that excess current did not burn out the sample. All the measurements were taken at biases as close to this compliance value as possible in order to maximise carrier concentration.

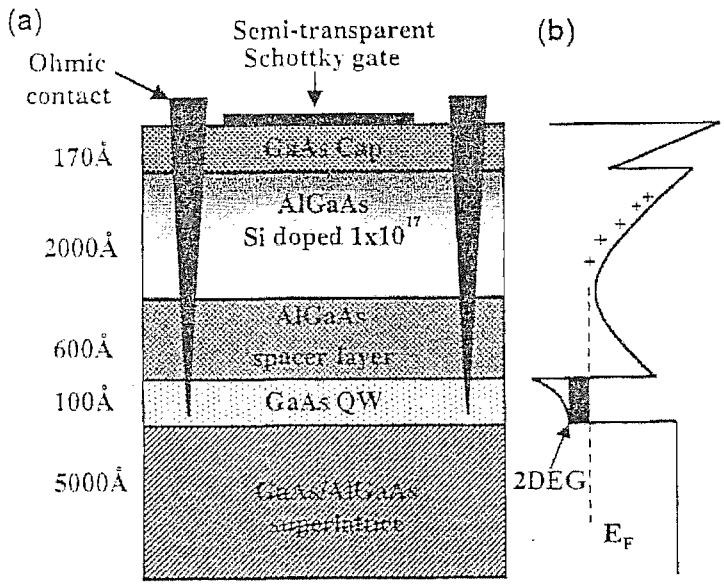

Figure 6.5. Diagram of the sample structure (a) and its conduction band profile (b). Excerpted from Kaur [9]

PL measurements (as described in section 4.4 above) were performed at temperatures between 10K and 275K. Time resolved measurements of the sum and

difference signals were taken (using the balanced detection system described in section 3.3) at temperatures between 10K and 275K.

6.3 Experimental Results.

This section shows the photoluminescence measurements for temperatures between 10k and 300K and measurements of the spin evolution at temperatures between 10K and 275K. Selected measurements of the carrier recombination time (the sum signal) will also be shown.

6.3.2 Photoluminescence Measurements.

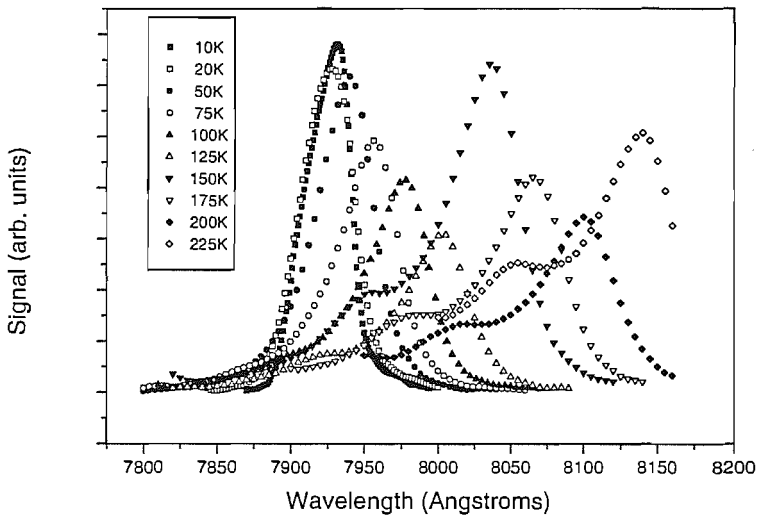

Figure 6.6a. Photoluminescence measurements for temperatures from 10K to 225K. The measurements were taken with a HeNe laser as excitation source at 632.8 nm. The largest (long wavelength) peak at each temperature is due to electron-heavy hole recombination. The low wavelength shoulder which appears at higher temperatures is due to electron-light hole recombination.

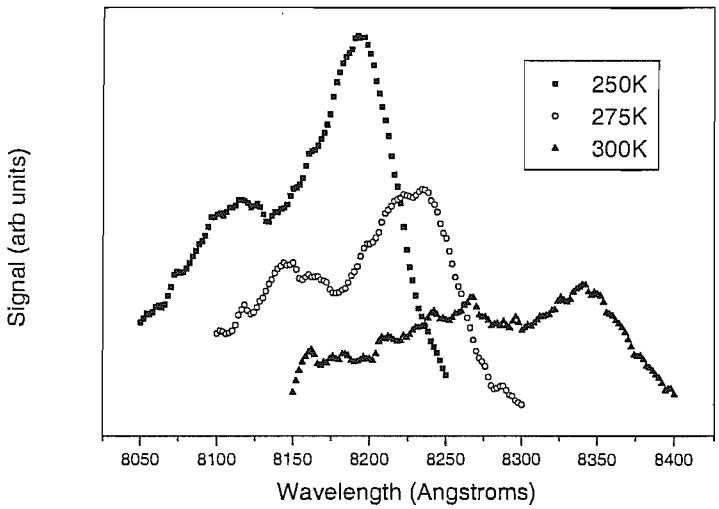

Figure 6.6b. Photoluminescence measurements for 250K, 275K and 300K.

6.3.1 Time Resolved Measurements.

Figures 6.7(a-m) show the spin evolution (difference signal) in the 2DEG at different temperatures. The pump power density for each case is specified. Figure 6.8 shows a typical example of the sum signal. The fact that this is essentially constant for delays from 0 to 150 ps indicates that the decay of the difference signal may be taken as a measure of the pure spin decay. The fits shown are single exponential fits derived using the Origin 5.0 program.

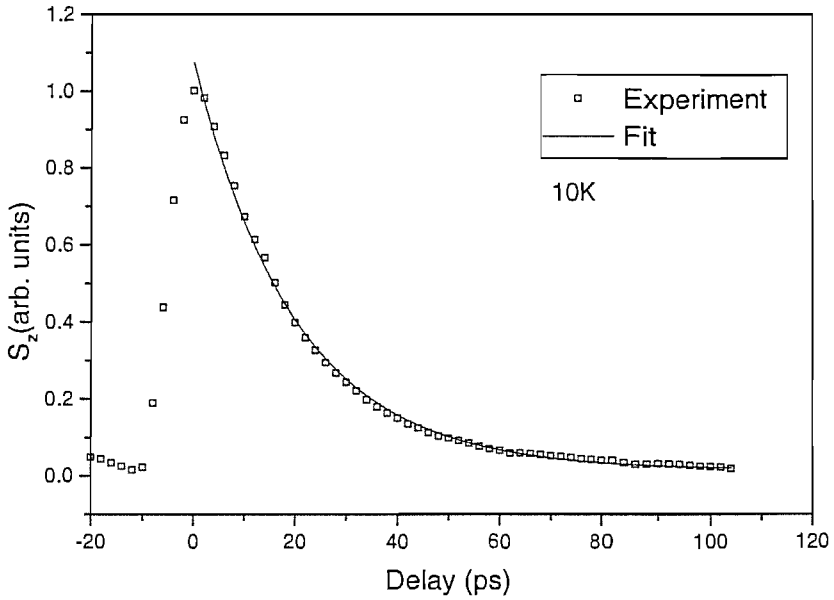

Figure 6.7a. Spin evolution at 10K (squares) with fit (curve) of decay time τ_s. The power density was 3.38 10^5 W m^{-2}.

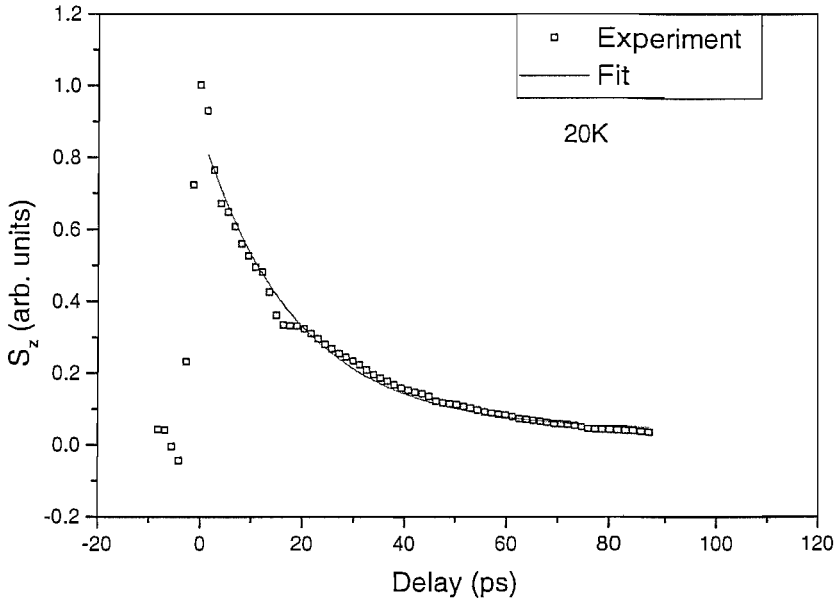

Figure 6.7b. Spin evolution at 20K (squares) with fit (curve) of decay time τ_s. The power density was 1.07 10^6 W m^{-2}.

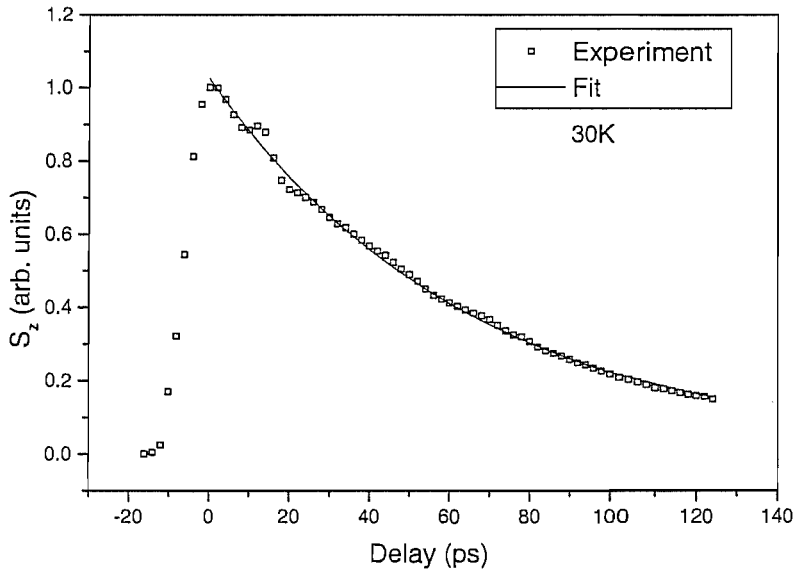

Figure 6.7c. Spin evolution at 30K (squares) with fit (curve) of decay time τ_s. The power density was 1.07 10^6 W m^{-2}.

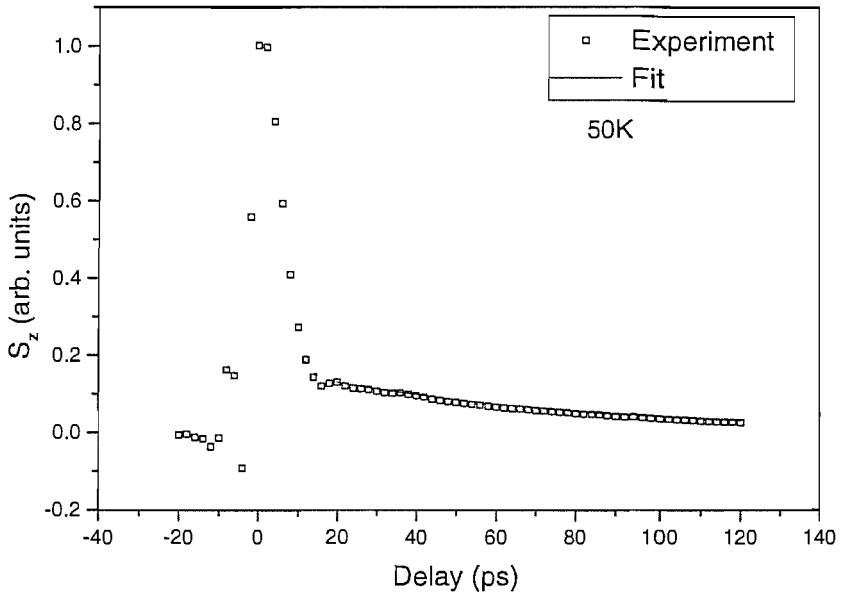

Figure 6.7e. Spin evolution at 50K (squares) with fit (curve) of decay time τ_s. The power density was 1.0710^6 W m^{-2}.

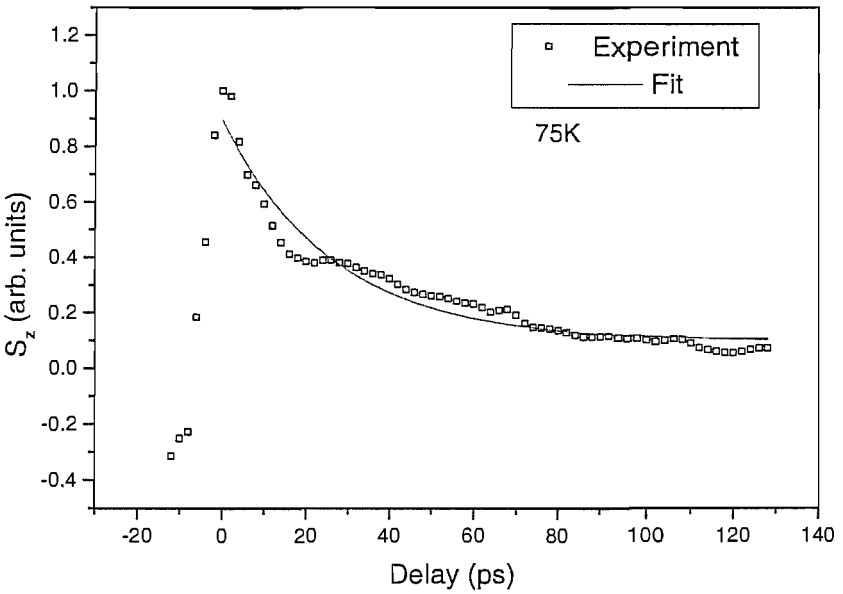

Figure 6.7f. Spin evolution at 75K (squares) with fit (curve) of decay time τ_s. The power density was $1.07*10^6$ W m^{-2}.

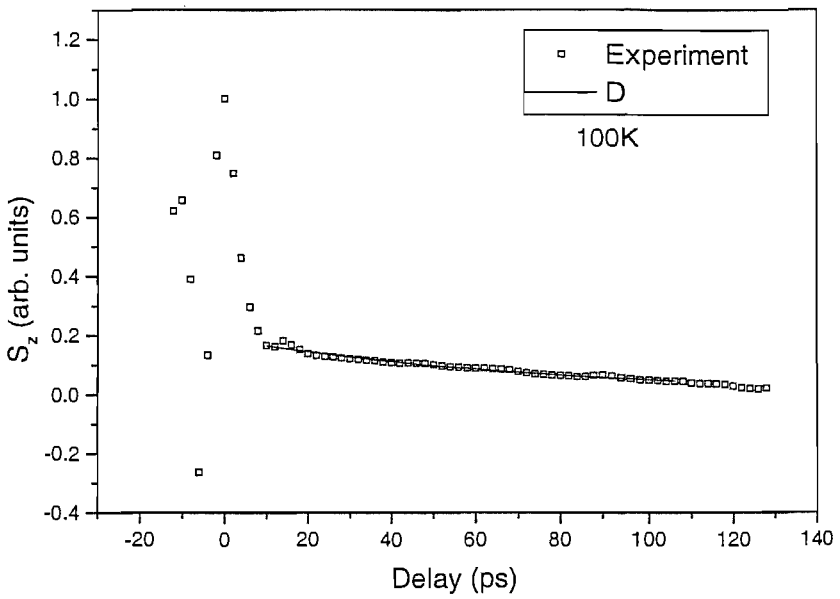

Figure 6.7g. Spin evolution at 100K (squares) with fit (curve) of decay time τ_s. The power density was $1.07*10^6$ W m^{-2}.

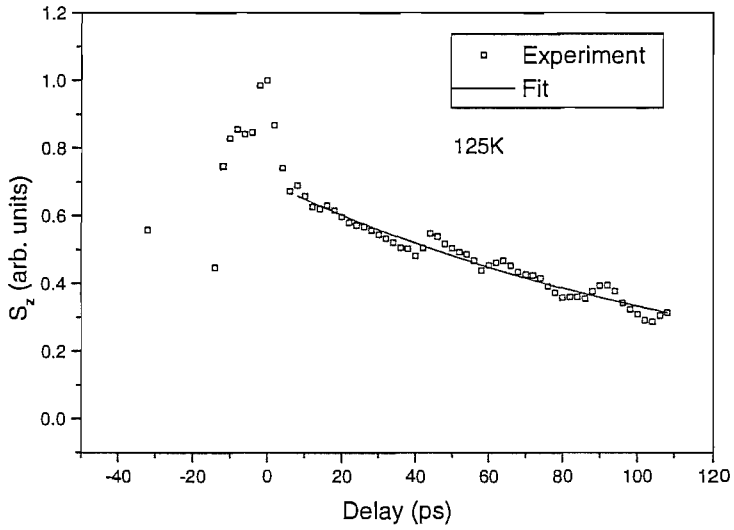

Figure 6.7h. Spin evolution at 125K (squares) with fit (curve) of decay time τ_s. The power density was $1.85*10^6$ W m^{-2}.

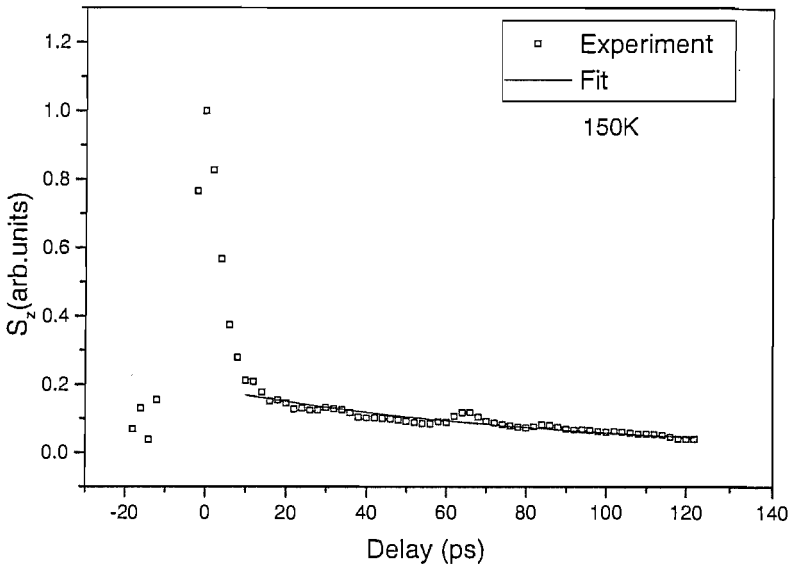

Figure 6.7i. Spin evolution at 150K (squares) with fit (curve) of decay time τ_s. The power density was $1.95*10^6$ W m^{-2}.

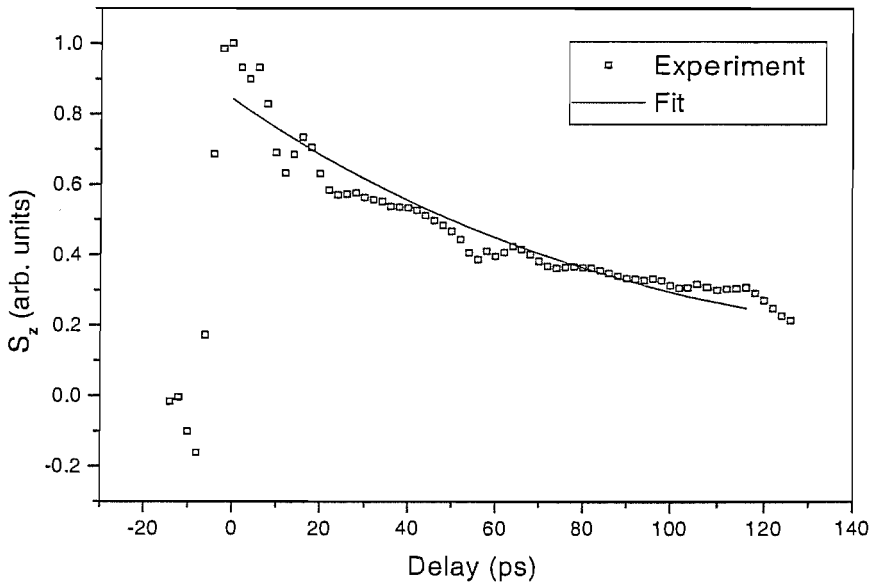

Figure 6.7j. Spin evolution at 175K (squares) with fit (curve) of decay time τ_s. the power density was $2.47*10^6$ W m^{-2}.

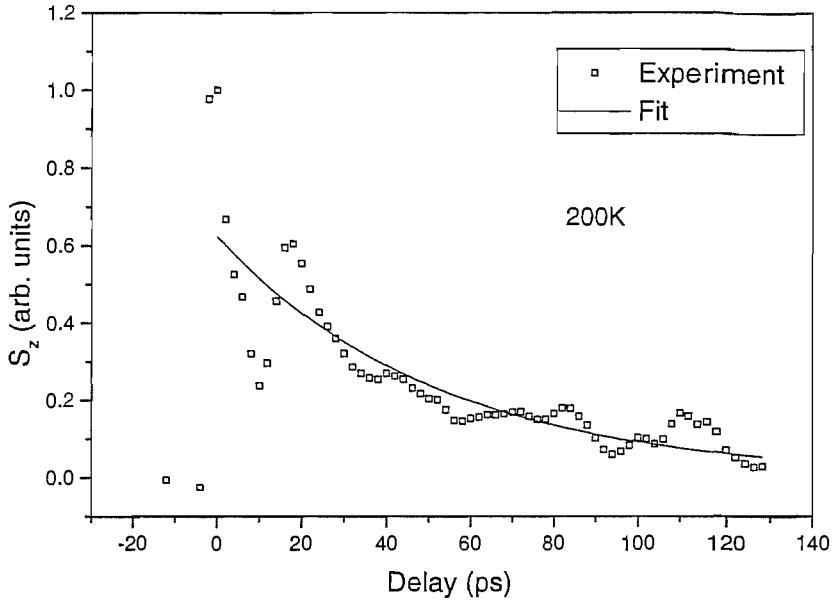

Figure 6.7k. Spin evolution at 200K (squares) with fit (curve) of decay time τ_s. The power density was $2.99*10^6$ W m^{-2}.

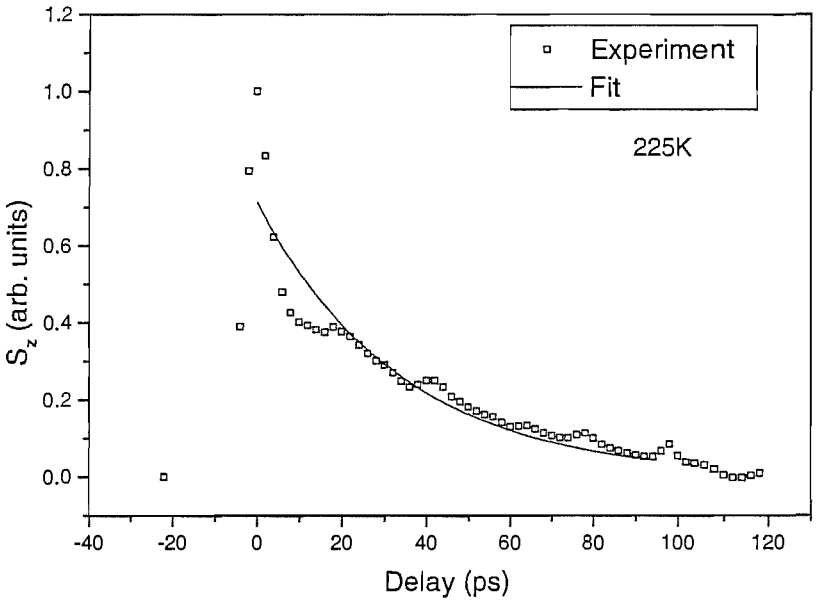

Figure 6.7l. Spin evolution at 225K (squares) with fit (curve) of decay time τ_s. The power density was $3.77*10^6$ W m^{-2}.

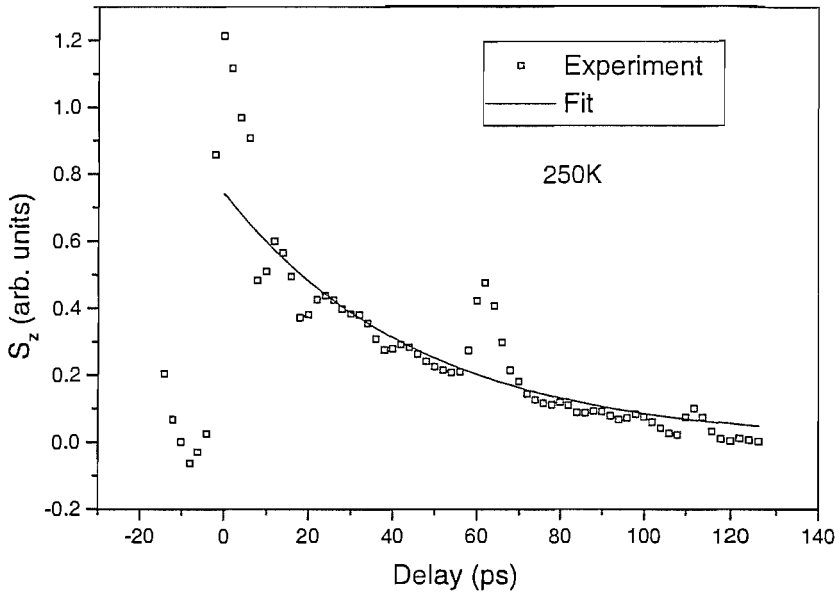

Figure 6.7m. Spin evolution at 250K (squares) with fit (curve) of decay time τ_s. The power density was $4.22*10^6$ W m^{-2}.

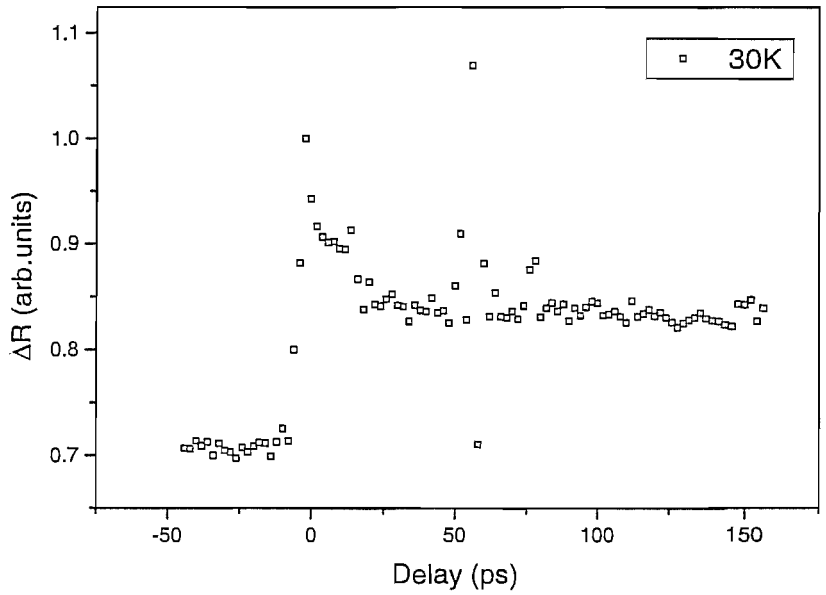

Figure 6.8. The change in reflectivity (ΔR) at 30K of the probe beam due to pump absorption. The signal at all temperatures was typically a step response. This therefore would have little impact on the final spin relaxation time derived from the difference signal.

6.4 Data Analysis.

The difference signal results were modelled using a single exponential decay and an offset to account for the background signal:

$$A_1 \exp[t/\tau_s] + A_2 \quad (6.24)$$

Each measurement of the difference and sum signals had appreciable background noise, which became more significant as the temperature increased. Its presence remains unexplained in detail. It is possible that this signal was due to reflections from the optics. Before zero delay, reflected pulses of the pump beam interfering with the probe pulses may give rise to peaks or background noise, whereas after zero delay reflections within the probe beam line interfering with the pump pulses may do likewise. A particularly clear example of a reflection within the probe line is seen in several traces at about 60 ps and is ignored in the analysis. This may also account for the noise seen immediately after zero delay. Steps were taken to eliminate this effect as far as possible by careful adjustment of the optical bench components. This problem could be further reduced by using optics with an anti-reflection coating but this was not practicable for the present experiments due to the time and expense required. The parameter A_2 was introduced to compensate for the background value. The intensity of the signal falls off with increasing temperature. The parameter A_1 is introduced to normalise the signals. The experimental data shown in figure 6.7(a-m) have had their background values A_2 subtracted and have been divided by value A_1.

The assumption that the spin relaxation time τ_s can be found by analysing the difference signal alone is not always correct. Strictly speaking, the spin relaxation rate

is found by subtracting the recombination rate (extracted from the decay of the sum signal) from the decay of the difference signal.

$$\tau_s^{-1} = \tau_d^{-1} - \tau_r^{-1} \quad (6.25)$$

However, the sum signal measured for this sample approximates to a step response, so that the recombination rate is so small that its contribution to the decay may be neglected and the spin relaxation rate is extracted from the difference signal only.

The spin relaxation rate as a function of temperature is shown in figure 6.9.

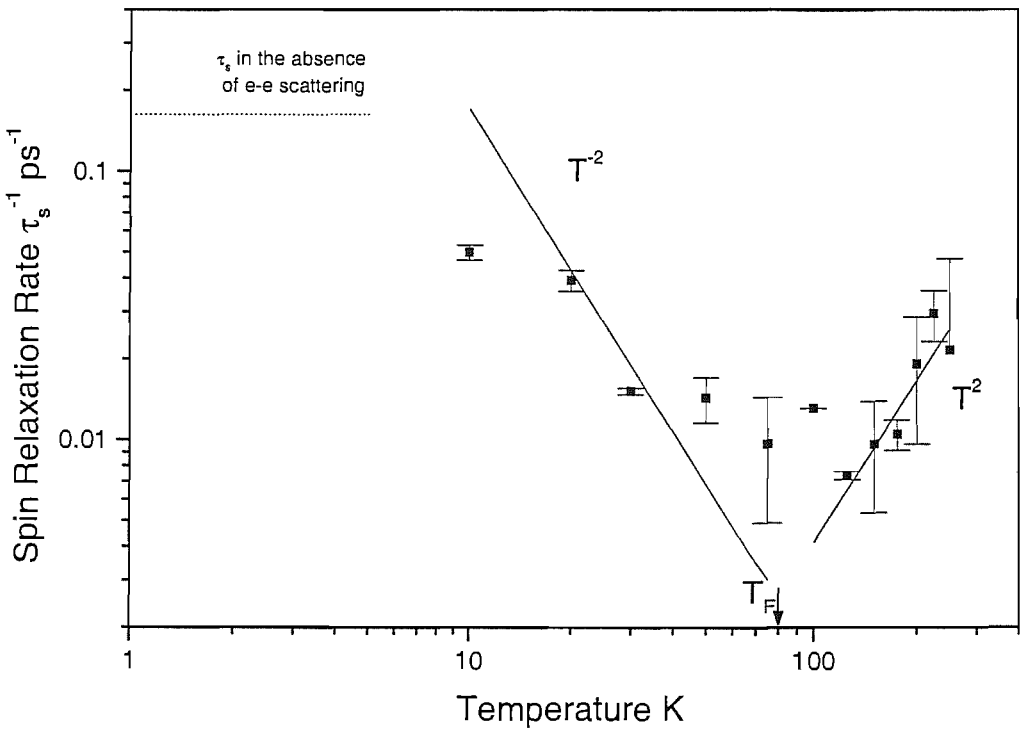

Figure 6.9. Log-log plot for spin relaxation rate τ_s^{-1} versus temperature. The T^{-2} dependence of the spin relaxation rate becomes less pronounced at low temperatures as electron-electron scattering becomes less frequent. The spin relaxation rate in the absence of electron-electron scattering is shown as a dotted line. Above the Fermi temperature T_F (shown as an arrow on the T axis) the spin relaxation rate has a T^2 dependence as optical phonon scattering becomes more pronounced. In the non-degenerate temperature region the temperature dependences of the mean square precession frequency and electron-electron scattering rate vary inversely to one another.

Figure 6.9 clearly shows both degenerate and non-degenerate regions, with the Fermi temperature at approximately 75-100K. The spin relaxation rate, at least qualitatively follows the dependence predicted theoretically with a minimum near T_F. Above 200K the signals associated with the 2DEG become too weak to measure.

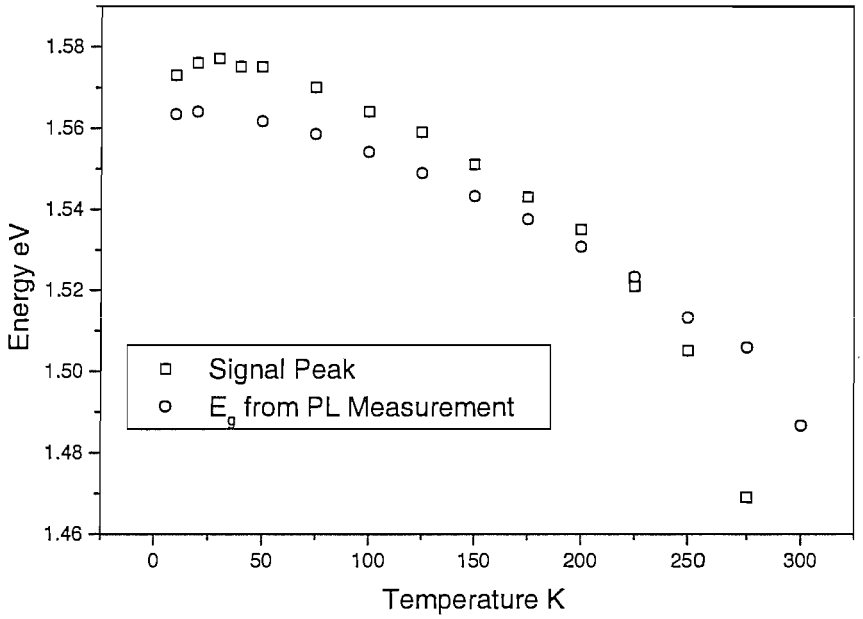

Figure 6.10. Comparison of the band gap energy (derived from photoluminescence measurements) with the energy at which measurements of the spin decay were taken.

Figure 6.10 shows a comparison at various temperatures of the energies of the photoluminescence peaks and the energy that gave the maximum time resolved signal at which the measurements of spin decay where taken. At low temperatures the time resolved signal shows a maximum at a significantly higher energy than the PL peak. This difference corresponds to the depth of the Fermi sea in the 2DEG plus the heavy-hole valence band dispersion up to the Fermi wavevector. At high temperatures the difference disappears, consistent with the transition to a non-degenerate Fermi gas of electrons.

6.4.1 Data Analysis with respect to the predictions of the D'yakonov-Perel Theory.

Referring back to the theory outlined at the beginning of this chapter (and covered briefly in section 2.3), the data is analysed with respect to the D'yakonov Perel equation:

$$\tau_s^{-1} = \langle\Omega^2\rangle\tau_p^* \qquad (2.1)$$

which may be rewritten as:

$$\tau_s^{-1} = \langle\Omega^2\rangle (\tau_p^{-1}+\tau_{ee}^{-1})^{-1} \qquad (6.1)$$

This section we will use values of the transport relaxation time τ_p obtained from mobility measurements together with theoretical estimates of $\langle\Omega^2\rangle$ to extract the electron-electron scattering time from the data presented above.

The values for the mean square precession frequency are taken from the work done by Brand (2003) which gives a method for calculating values up to 300K (see figure 6.11a). This method consists of averaging the spin splitting over the photoexcited electron spin population, assuming that there is full thermalisation within the pulse duration.

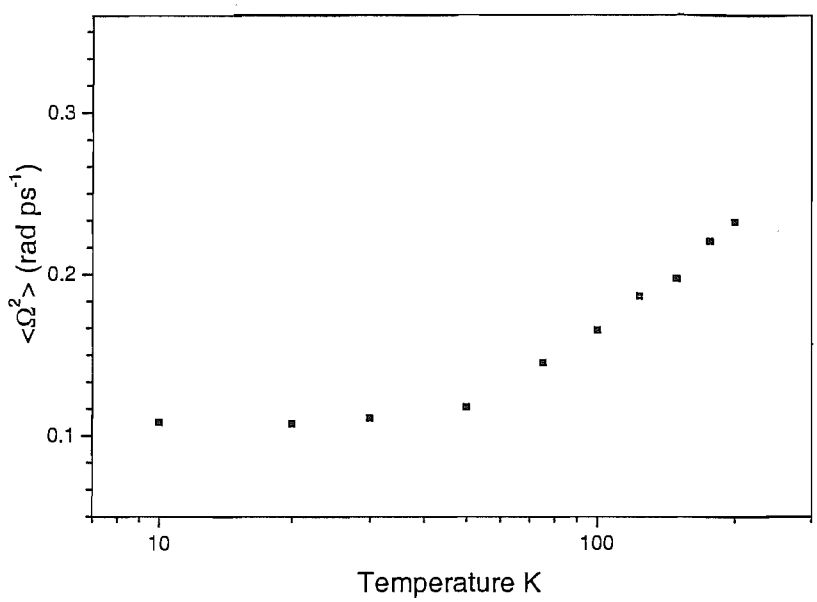

Figure 6.11a. Mean square precession frequency versus log temperature. The precession is independent of temperature below the Fermi temperature but follows a linear dependence above T_F.

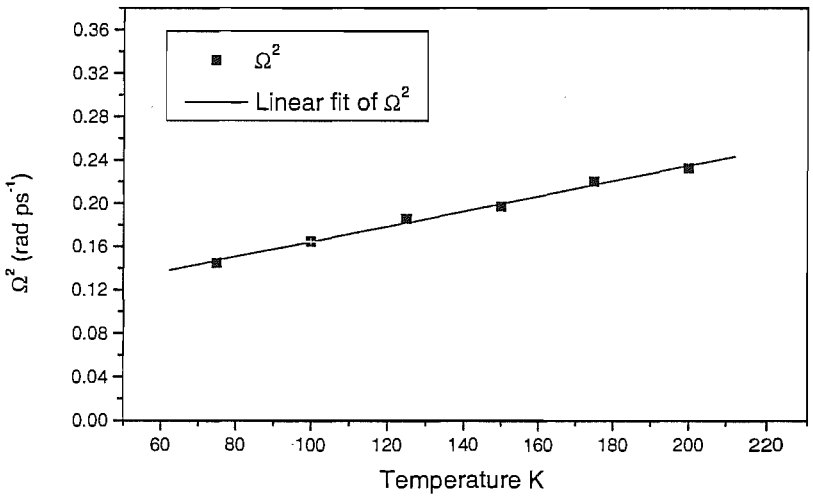

Figure 6.11b. Linear fit of mean square precession frequency versus temperature for temperatures above T_F. A linear relationship between temperature and Ω^2 is clearly apparent.

Using these values, it is possible to extract values of the momentum relaxation time τ_p^* by dividing the spin relaxation time by the mean square precession frequency (see figure 6.12)

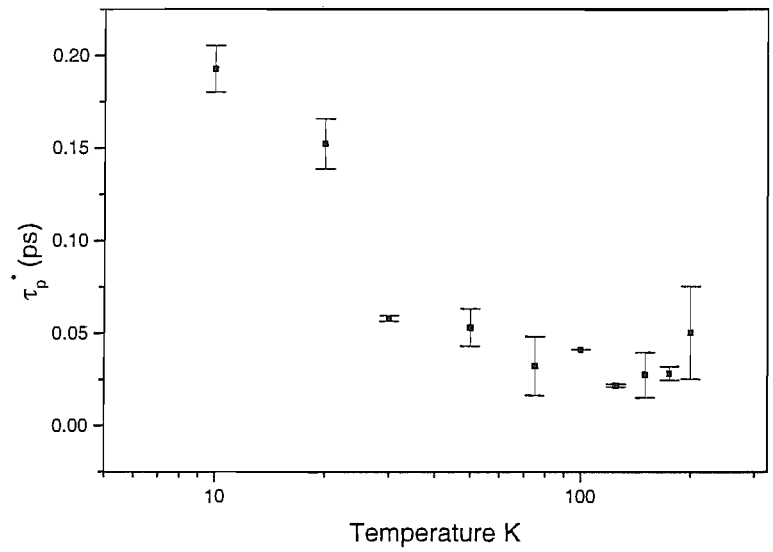

Figure 6.12. Momentum relaxation time as a function of temperature.

Hall effect measurements (see section 4.6) were performed to find values for the mobility. This was used to calculate values of the transport relaxation time, using the equation $\mu = e\tau_p/m_e^*$. The reduced mass $m_e^* = 0.067m_e$. The results of this are shown in figure 6.13a.

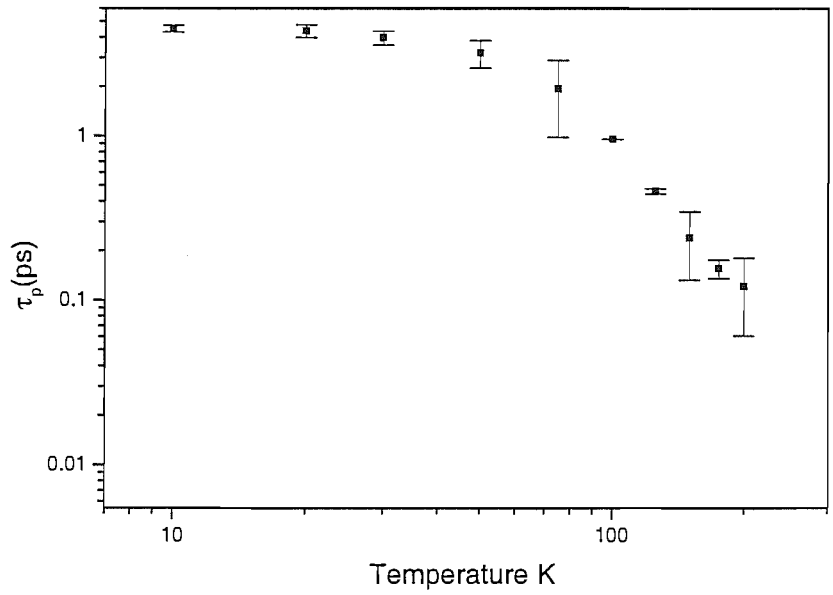

Figure 6.13a. Transport relaxation time as a function of temperature.

In order to test the assumptions made at the beginning of this chapter, it is necessary to examine the temperature dependence of the transport relaxation rate.

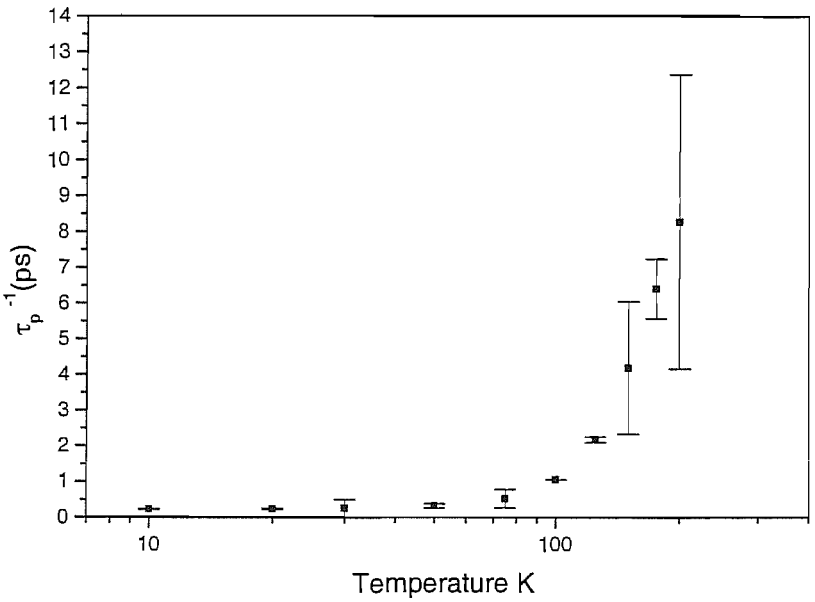

Figure 6.13b. Transport relaxation rate as a function of temperature. The lack of any variation in the low temperature region is due to the lack of impurity scattering and low thermal scattering (see section 6.1)

It can be seen that up to 100K, corresponding to the degenerate state there is little temperature dependence of the spin relaxation rate. However, analysis of the spin relaxation rate above T = 100 K could be described as showing the predicted T^2 dependence from equation 6.24 (see figure 6.13c) but could also fit to a T dependence, or be independent of T. More work to investigate this area is being performed by Professor Richard Harley.

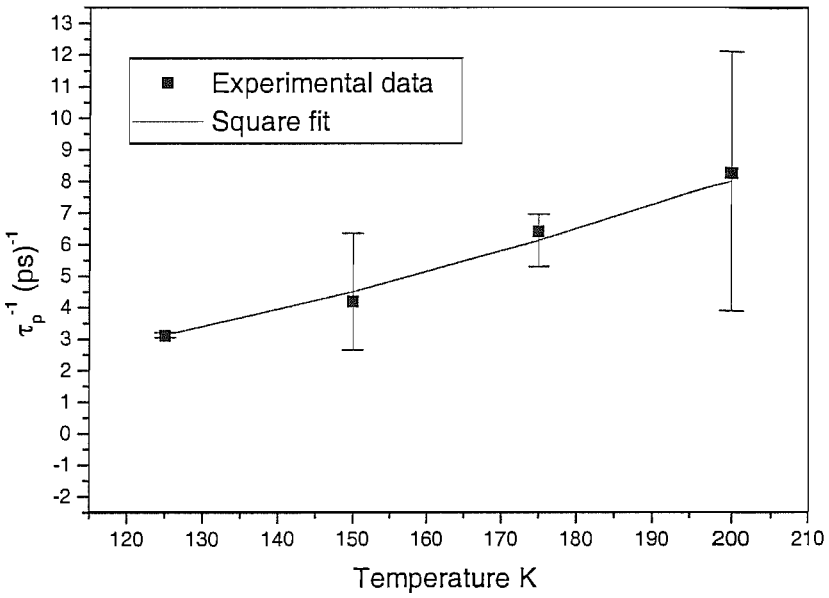

Figure 6.13c. Experimental results for transport relaxation rate, fitted for a T^2 dependence.

The contribution of the electron-electron scattering may be found by subtracting the transport relaxation rate from the momentum relaxation rate. The result is shown in figure 6.14a.

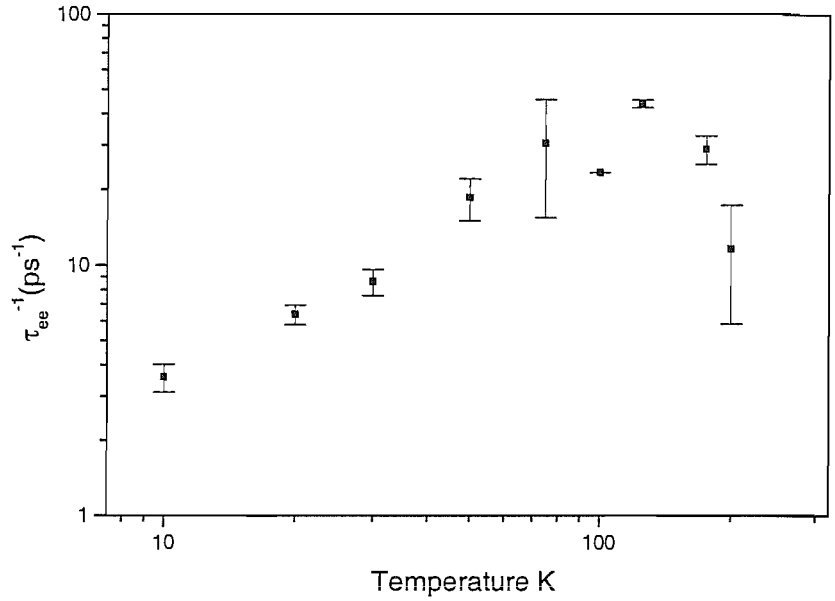

Figure 6.14a. Extracted values for electron-electron scattering rate.

These results were then analysed to find the temperature dependence of the electron-electron scattering rate in the degenerate and non-degenerate regions.

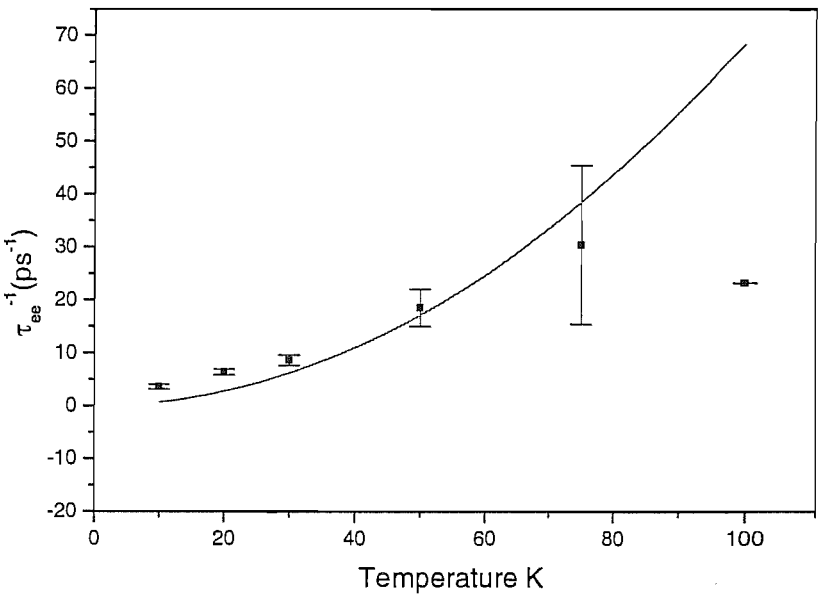

Figure 6.14b. Square fit for electron-electron scattering rate in the degenerate case.

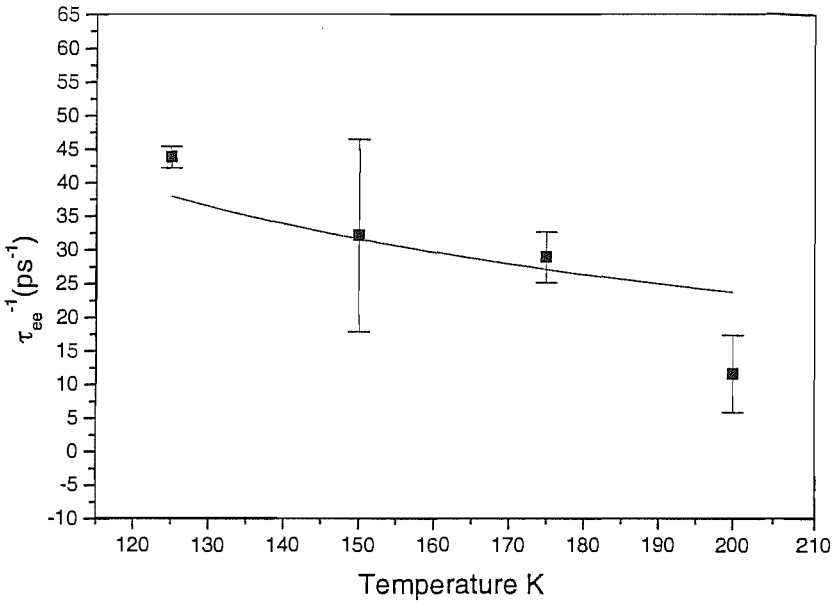

Figure 6.14c. Inverse temperature dependence fit for the electron-electron scattering rate in the non-degenerate case.

The attempted fit for the degenerate case is not precise as it fails to take into account the decreasing strength of electron-electron scattering at temperatures below ~10K. The linear fit for the data in the non-degenerate case is a weak fit due to the decrease in signal strength (and hence resolution) with increasing temperature.

6.5 Conclusion.

The results shown above clearly follow the predictions of the D'yakonov Perel theory on the spin relaxation. It may also be seen that predictions regarding the electron-electron scattering rate in the degenerate region also correspond with the theoretical predictions. However, the predictions regarding the non-degenerate region are still tentative. Firm evidence for these predictions may be found once more accurate data for temperatures $\geq$ 225K are obtained. Recent data obtained by Professor Richard Harley suggest that this is the case, and that the spin relaxation rate continues to increase in the non-degenerate region up to room temperature. However, the temperature results also confirm the data found by Brand [6] and suggest that the spin decay is mostly affected by the electron-electron scattering.

6.6 References.

1. "Spin-orbit coupling effects in zincblende structures," G. Dresselhaus, Phys. Rev. **100** 580 (1955).
2. "Precession spin relaxation mechanism caused by frequent electron-electron collisions," M. Glazov and E. L. Ivchenko, JETP Letters, **75** 403.
3. "Low Temperature Solid State Physics," H. M. Rosenberg, Clarendon Press, Oxford, (1963).
4. "Quantum Semiconductor Structures, Fundamentals and Applications," C. Weisbuch and B. Vinter, Academic Press Inc., Boston. (1991).
5. "Spin relaxation of conduction electrons in noncentrosymmetric semiconductors," M. I. D'yakonov and V. I. Perel, Sov. Phys. JETP **33** 1053 (1971).
6. "Spin relaxation of two-dimensional electrons in noncentrosymmetric semiconductors," M. I. D'yakonov and V. Yu. Kachorovskii, Sov. Phys. Semicond. **20** 110 (1986).
7. "Coulomb scattering lifetime of a two-dimensional electron gas," L. Zheng and S. Das Sarma, Phys. Rev. B **53** 9964, (1996).
8. "Optical time resolved spin dynamics in III-V semiconductor quantum wells," M. Brand, PhD thesis, University of Southampton, (2003).
9. "Excess carrier Effects on the Optical emission and excitation Spectra of GaAs Quantum wells," R. Kaur, PhD thesis, Hughes Hall College, University of Cambridge, (2001).
10. "Electron temperature in a quantum well. Energy losses on quantum phonons." Esipov and Levinson, JETP Letters, **42**, 193, (1985).

CHAPTER 7.

CARRIER CONCENTRATION DEPENDENCE OF SPIN RELAXATION TIME IN A MODULATION DOPED QUANTUM WELL.

7.1 Introduction.

The spin relaxation rate in a 2DEG is expected to be dependent upon carrier concentration, in the manner set out in chapter 6. To recap from section 6.1, in the degenerate case, the mean square precession frequency is linearly dependent on the concentration:

$$<\Omega^2> \sim E_{le}^2 N_s$$

In the high temperature regime thermalisation dominates and k_BT becomes larger than E_F. (The Fermi level is determined by the electron concentration.) Consequently the mean square precession frequency becomes independent of concentration.

In the degenerate case, the electron-electron scattering rate follows concentration dependence.

$$\tau_{ee}^{-1} \sim N_s^{-1} T^2$$

so that the spin relaxation time should be proportional to N_s^{-2}. In the high temperature, non-degenerate regime the electron-electron scattering rate is

$$\tau_{ee}^{-1} \sim N_s T^{-1}$$

so that the spin relaxation time should be directly proportional to N_s.

In this chapter we will describe work intended to examine this dependence at 10K and 20K, i.e. in the degenerate regime.

7.2 Experimental Method.

The experimental set up was the pump probe geometry described in section 4, using the flow cryostat. A Source Measure Unit (SMU) was used to bias the sample

and hence vary the carrier concentration in the well. Electroreflectance measurements for each bias value were taken. This gives a measure of the Fermi level of the 2DEG. Combined with the measurements of the PL this gives a determination of the carrier concentration. Time resolved measurements were taken at the peak of the ER (and hence the top of the Fermi sea) to investigate the spin decay.

7.3 Results.

Preliminary measurements of the spin decay at 10K and 20K were taken for different biases. It was thought, that, as the bias was reduced, the Fermi level would shift, so the measurements at low bias were no longer being conducted at the Fermi edge. Measurements of the electroreflectance spectrum were therefore performed in order to investigate the change of the Fermi level as the bias was reduced. (These measurements are preferable to PLE measurements because the sample is in the same geometry as for spin decay measurements, whereas a change in geometry would be required between PLE and spin decay measurements.)

The results display a shift in the Fermi peak to lower energies as the bias is reduced. This is because, at lower biases (and hence carrier concentrations) there are fewer electrons in the conduction band. Of more profound interest, however, is how the shape of the ER spectrum changes as the well is depopulated. (See figure 7.1 and 7.2 for examples of ER spectra at 10K and 20K respectively.) Peaks appear at three separate energies as the bias is reduced. This is due to excitons appearing in the well.

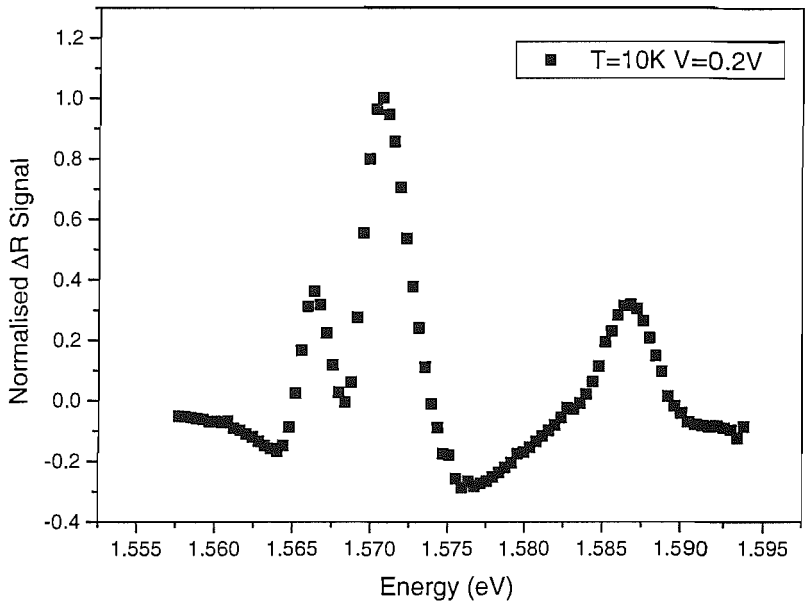

Figure 7.1. Typical electroreflectance spectrum for 10K at intermediate bias. The three peaks represent, from left to right, neutral exciton, negatively charged exciton and light hole.

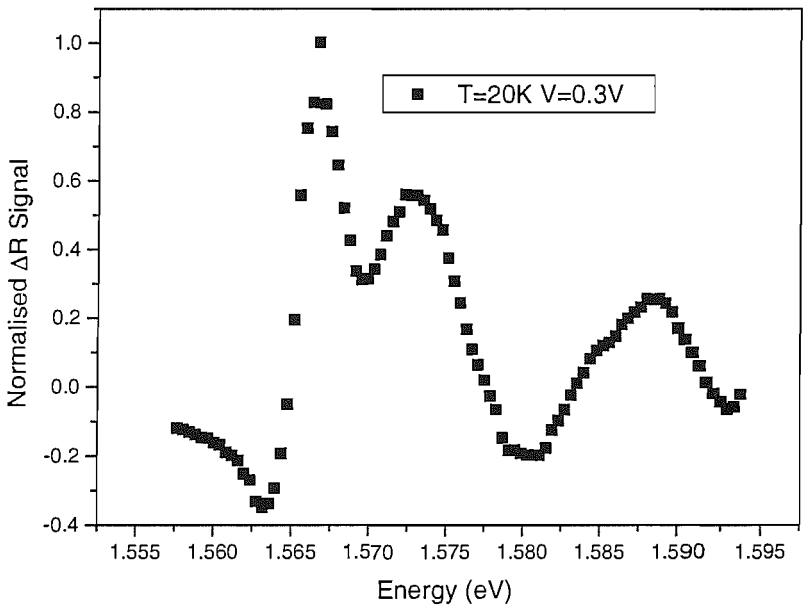

Figure 7.2. Typical electroreflectance spectrum for 20K at intermediate bias. The three peaks represent, from left to right, neutral exciton, negatively charged exciton, and light hole.

At high gate biases, the electron concentration in the well is enough so that a 2DEG exists. However, at lower gate biases fewer free electrons are injected into the

well and electrons and holes may combine to form excitonic bound states. At electron concentrations ~ 10^{10} cm^{-2} two electrons tend to bind with a hole to form a negatively charged exciton, X^-.[2] At biases below ~ 0.6V the TR and ER results suggest that free electrons are no longer the predominant charge carrier, and that excitons then predominate. As the well is further depleted, the predominant form of charge carriers shifts from negatively charged excitons to neutral excitons.

7.3.1 Energy levels of the bound state.

There are three absorption thresholds observable in the ER spectrum. These correspond to the doubly, singly and unoccupied states. This represents, respectively, two (X^-), one (X) and zero (e) electrons bound to a hole.

Figure 7.4 shows the absorption spectra for the bound and continuum states, where $\hbar\omega_3$ represents the energy of the continuum, $\hbar\omega_2$ represents the energy of the first bound state, i.e., the neutral exciton and $\hbar\omega_1$ represents the energy of the second bound state, i.e., the negatively charged exciton. As the gate bias increases, more electrons are introduced into the well. Once electron concentration is of the order ~10^{10} cm^{-2}, these excess electrons will bind to a neutral exciton and create a negatively charged exciton X^{-1}.

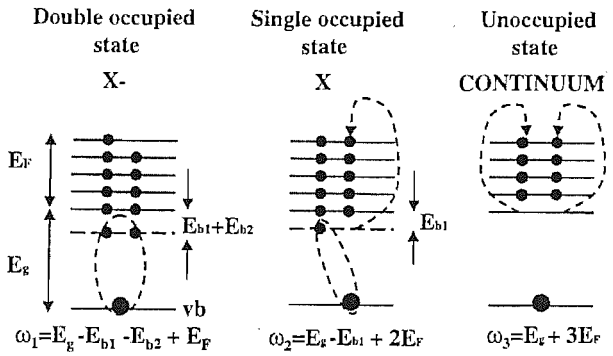

Figure 7.4 Three different occupied and unoccupied states. Excerpted from Kaur [3].

The energy of the states is determined by the number of electrons bound by the Coulomb attraction to the photo-excited hole. As may be seen in figure 7.4, to create a doubly occupied state, two electrons are excited from the valence band to the top of the conduction band and then relax to the bottom of the conduction band to form the negatively charged exciton. If one of the electrons in this bound state is then excited to the top of the conduction band by applying energy E_F, the singly occupied state, or neutral exciton is formed. If the remaining electron in the bound state is excited to the top of the conduction band, there is no occupied state and an electron continuum exists. The predicted energies, according to Kaur [2]; are:

$\hbar\omega_1 = E_g - E_{b1} - E_{b2} + E_F$

$\hbar\omega_2 = E_g - E_{b1} + 2E_F$

$\hbar\omega_3 = E_g + 3E_g$

At higher concentrations, there are no free holes and only the continuum is evident. The negatively charged exciton threshold then turns into the Fermi-edge singularity. Shields et al [3] suggest that in the case of the negatively charged exciton the additional spin of the hole results in a two fold degenerate ground state, which they refer to as a singlet X^-_s. They also refer to a six fold degenerate triplet state X^-_t. However, this is only observable under the application of a magnetic field above 4 T, and at zero magnetic field is not optically distinct.

The 2K data obtained by Kaur [4] shows two shoulders on the high energy side of the PL. The 10K and 20K data shown in chapter 6 also show slight evidence of these features.

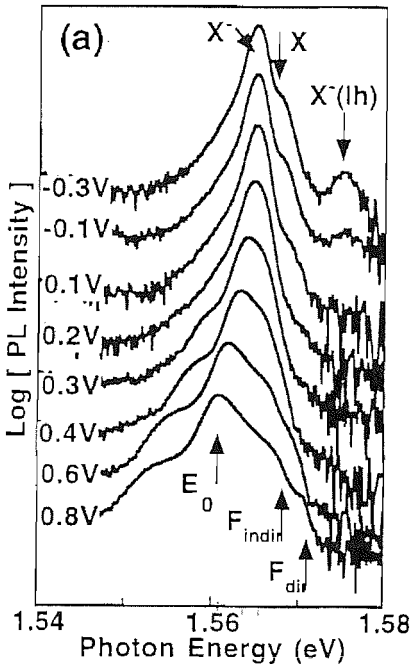

Figure 7.5 2K PL. Excerpted from Kaur [3].

The low energy shoulder is due to the recombination of the electrons at the Fermi wave vector with holes at k = 0. This recombination occurs due to interface roughness scattering. It can be inferred that this shoulder is not due to a k-conserving recombination from the top of the Fermi sea because it does not correspond to the peak of the ER spectrum.

The figure above shows the PL as a function of gate bias for biases from -0.3V to 0.8V. As the well is depopulated by reducing the gate bias, the peak (corresponding to the band gap E_g) shifts towards higher energy. This is due to a reduction of the quantum confined Stark effect. As the bias is reduced the shoulder disappears and two peaks emerge. These peaks correspond to the neutral and negatively charged excitons. The separation of these two peaks corresponds to the binding energy of the second electron E_{b2}. The electroreflectance spectra that were measured for all biases from 0.8V to -0.3V were compared with the PL to find values of carrier concentration from

the Stokes shift. (The carrier concentration may also be found by comparing the peak of the PL with the low energy shoulder corresponding to the indirect transition F_{indir}. However, this shoulder is only visible at high biases.)

7.3.2 Energy levels of the exciton

Figure 7.6 a and b show the values for the three different absorption thresholds for 10K and 20K as a function of bias. The threshold values are derived from the electroreflectance results and the concentration values are derived from the separation of the PL peak (found in Kaur and Shields's data) and the peak of the electroreflectance spectra. The value of carrier concentration is hence derived from the depth of the Fermi sea.

$E_{(ER\text{-}PL)} = (m_e^{*-1} + m_h^{*-1})\ (\hbar^2 k_F^2)/2$

Where $(m_e^{*-1} + m_h^{*-1}) = \mu_{ex}^{-1}$ inverse of the exciton effective mass

$E_F = (\hbar^2 k_F^2)/2\ m_e^*$

$N_s = \rho E_F = E_F\ m_e^*/(\pi\hbar^2)$

$= k_F^2/2\pi$

Therefore $k_F^2 = 2\pi\ N_s$

$E_{(ER\text{-}PL)} = \hbar^2\pi\ N_s(m_e^{*-1} + m_h^{*-1})$

$N_s = E_{(ER\text{-}PL)}\ \mu_{ex}\ (\pi\ \hbar^2)^{-1}$

Assuming that, according to Plaut [5] $\mu_{ex} = 0.046\ m_e^*$,

Then $N_s = 1.897*10^{14}$ per meV difference between the ER and PL peaks.

The lowest energy found in the negative exciton threshold closely follows the peak of the k-conserving energy peak found in Kaur's PL results. This emphasises that the negatively charged exciton at low carrier densities evolves into the Fermi-edge singularity. At high concentrations it may be seen that the peak of the supposed negative exciton absorption ceases to follow a regular gradient. It may be deduced

that this is due to the increased carrier concentration allowing the free electrons to predominate and the bias keeping the electrons and holes and different sides of the well.

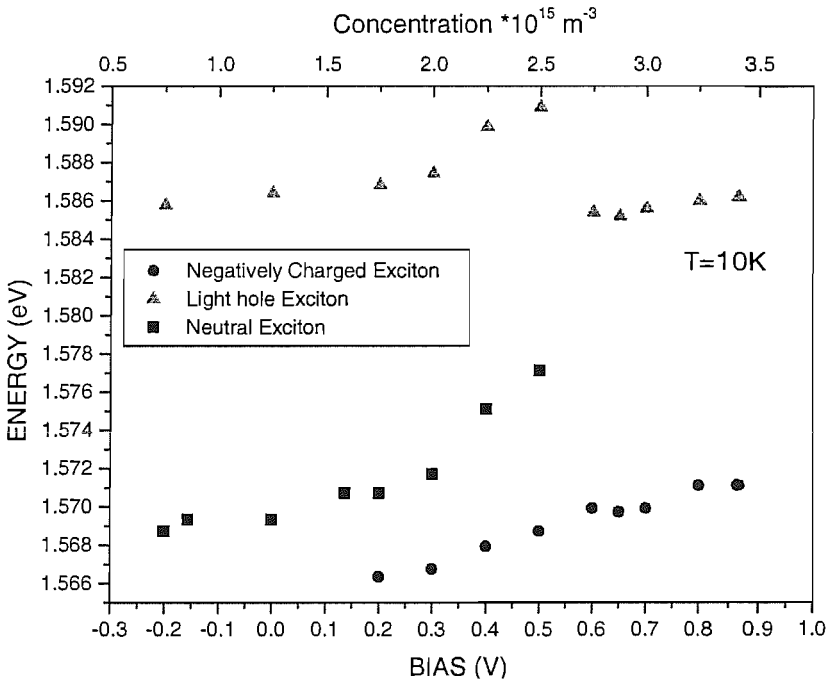

Figure 7.6a Absorption peaks as a function of bias at 10K. The concentration measurements are derived from the Stokes shift between the PL and ER measurements.

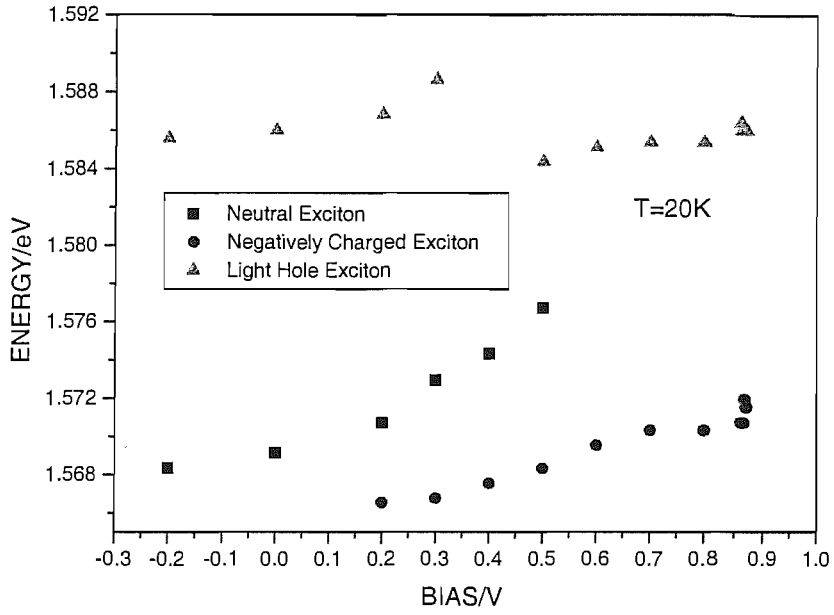

Figure 7.6b Absorption peaks as a function of bias at 20K.

It may be seen in figures 7.6a and b that there is a discontinuity in the gradient of the light hole peaks. This would correspond to light hole negatively charged and neutral excitons.

7.3.3 Spin dynamics of the exciton.

The spin dynamics of an electron system are modified when conditions favour the formation of excitons, with the most obvious effect being the exchange enhancement of spin decay due to the close proximity of the electron and hole constituents and the inhibition of hole spin relaxation by the exchange splitting.

The z-component of spin angular momentum of a neutral exciton J_z^{ex}, is equal to the sum of its constituents, S_z and J_z^h, where S_z and J_z^h are the z-components of the electron and hole spin angular momentum, respectively. Four spin configurations of the heavy hole angular momentum are possible:

J_z^h	S_z	J_z^{ex}
+3/2	+1/2	±2
+3/2	-1/2	±1
-3/2	+1/2	±1
-3/2	-1/2	±2

According to optical selection rules, (see section 2.2) only the $J_z^{ex} = \pm 1$ states can couple to light in a single photon process. This gives a limited range of spin transitions. The spin polarisation of the neutral excitons may diminish by either an independent single particle spin flip of the electron or hole constituent to form optically inactive neutral excitons of spin state $|\pm 2\rangle$, or via a simultaneous electron-hole spin flip which arises from the close spatial proximity of the electron and hole mediated by the exchange interaction and generates oppositely polarised, optically active excitons of spin state $|\pm 1\rangle$.

Spin relaxation of holes in III-V semiconductors is determined by the combination of valence band mixing and momentum scattering. In general it is usually assumed that the spin relaxation time of holes is much faster than that of electrons, although this may not hold true at low temperatures. In bulk materials or wide quantum wells, the strong valence band mixing near $\mathbf{k}=0$ causes rapid hole spin relaxation. Lifting of the lh-hh degeneracy (described in section 2.3) and displacement of the mixing to higher wave-vectors by quantum confinement increases the hole spin relaxation time considerably and for holes which remain at $\mathbf{k}=0$ the hole spin relaxation time is theoretically infinite. However, at low temperatures, the binding energy of the exciton is strong and coupled electron spin flip mechanisms are more important than these single particle processes. Maialle et al [5] consider the exciton

spin dynamics as having two parts, arising from the long range component and a short range component of the electron hole exchange interaction. The short range component depends upon the coupling of light and heavy hole states. This conserves total spin in the and so forbids a direct transition between the two optically active heavy hole exciton spin states, |3/2, -1/2> and |-3/2, 1/2>. A two step process for spin flip can take place:

$$|3/2, -1/2\rangle \rightarrow |1/2, 1/2\rangle \rightarrow |-3/2, 1/2\rangle$$

In the long range interaction, gives off diagonal elements in the Hamiltonian of the system which may be considered as an effective magnetic field in the xy plane that depends upon the wavevector of the exciton. The spin can then be thought of as precessing about this internal field, in an analogous manner to the DPK mechanism. As in the case of the DPK mechanism, collisions reduce the relaxation rate. The spin relaxation rate is then directly proportional to the mean square frequency of the precession, and is also directly proportional to the exciton momentum scattering time.

$$\tau_s(ex)^{-1} = \langle\Omega_{ll}^2\rangle\tau_p^* \text{ [5].}$$

Where $\tau_s(ex)^{-1}$ is the spin relaxation rate of the exciton, Ω_{ll}^2 is the mean square precession frequency around the internal field and τ_p^* is the momentum relaxation time.

Maialle et al [5] also introduce an equation for determining the individual transition rates for the electron and hole within the exciton.

$$W_{e,(h)}^{\pm} = \tau_{e,(h)}.[1+\exp(\pm\Delta_h/k_BT)]$$

Where $\tau_{e,(h)}$ is the single particle spin flip time of the electron or hole when bound in an exciton state and $W_{e,(h)}^{\pm}$ is the rate of electron or hole spin flip which results in the transition between exciton states. Δ_h is the energy of the optically active exciton states above the optically inactive states. Whether the spin relaxes with a single or double

exponential decay depends upon the relative sizes of the exciton transition rate and the individual electron and hole transition rates. That is to say, whether the spin relaxation involves spin flip of the exciton or spin flip of the individual electron and hole.

It is difficult to determine at what bias the 2DEG exists by examining the absorption spectra. This is because the negatively charged exciton absorption peak develops into the Fermi-edge singularity as the bias is increased. However, it is possible to view the change from one state to another by observing how the decay time varies as a function of bias. (See figures 7.7 and 7.8).

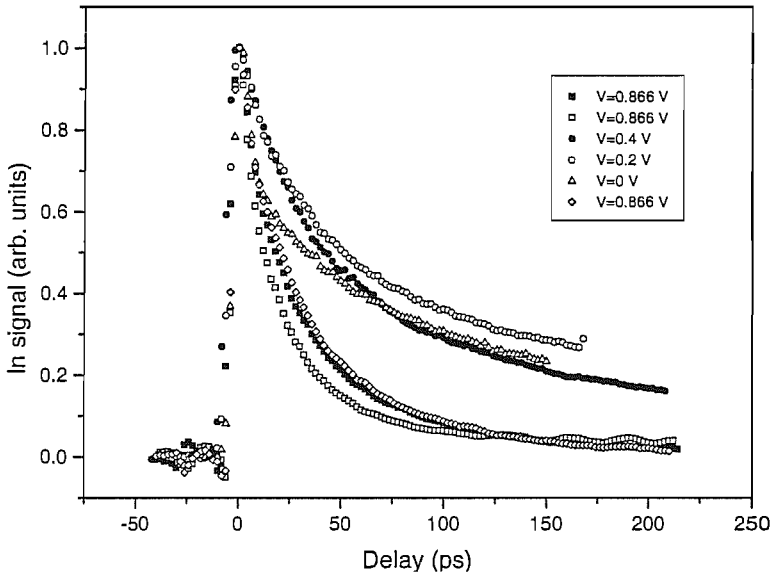

Figure 7.7. Spin relaxation at 10K as a function of bias

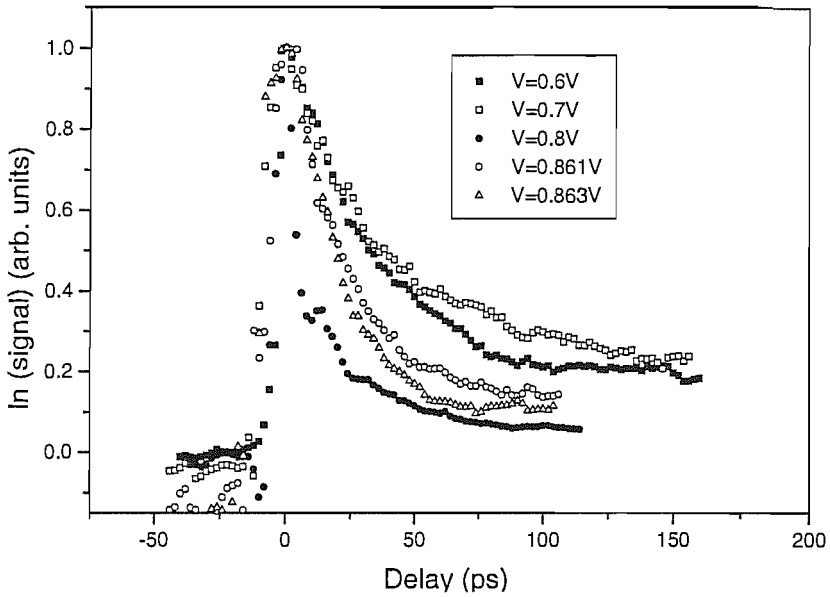

Figure 7.8. Spin relaxation at 10K as a function of bias. Higher bias values at the Fermi edge singularity shown for clarity.

At 10 K the spin relaxation time only follows the predicted spin dependence until the concentration reaches ~ 10^{10} cm^{-2}. At this point negatively charged excitons form at the Fermi edge singularity. Measurements of the spin relaxation time were taken at the negatively charged peak of the electroreflectance spectra. (See figures 7.9 and 7.10).

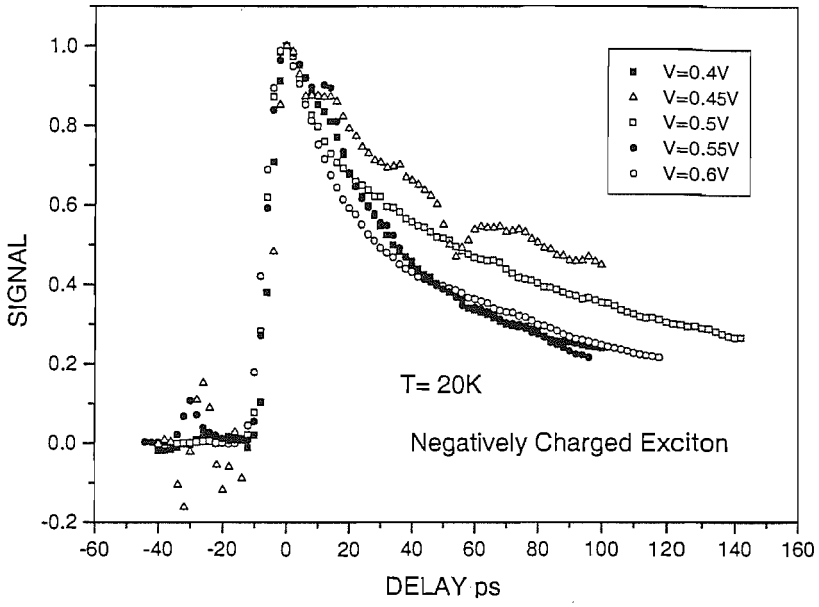

Figure 7.9. Spin relaxation measured at the negatively charged exciton as a function of bias at 20K.

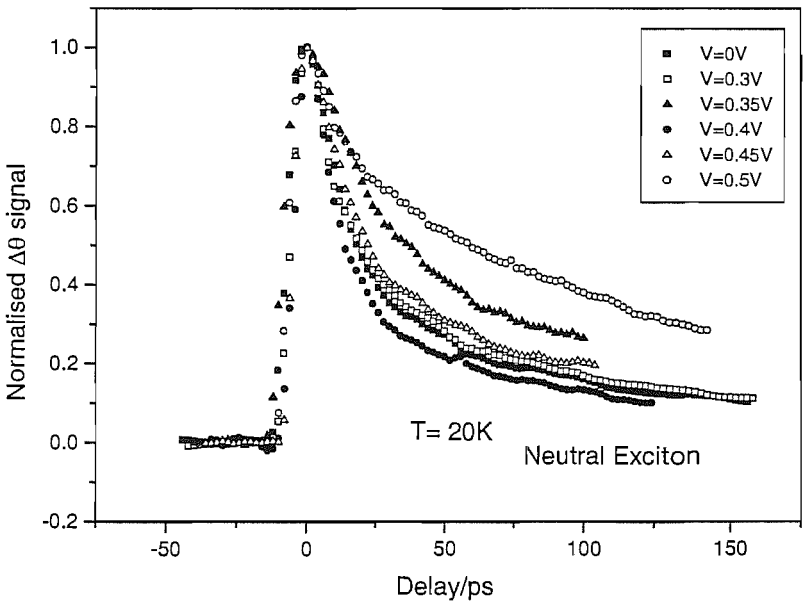

Figure 7.10. Spin relaxation at the neutral exciton peak of the electroreflectance spectra as a function of bias at 20K.

At low biases (-0.2V, 0V) the well is largely depleted of free electrons and the charge carriers are predominantly neutral excitons. As more electrons enter the well at higher biases negatively charged excitons are formed. The picture here becomes more complicated, as, according to Shields et al, there exists a triplet spin state for the

negatively charged exciton. At magnetic fields above 2T this is observed in the PL at energy higher than that of the normal negatively charged exciton singlet peak but lower than that of the neutral exciton peak. However, at zero field the triplet peak exists at the same energy as that of the neutral exciton. Therefore, it is difficult to analyse spin decay data at intermediate carrier densities due to problems in determining whether this data corresponds to neutral excitons or the triplet state of negatively charged excitons. Therefore, only limited data can be found from measurements made from the higher energy peak. (See figure 7.11)

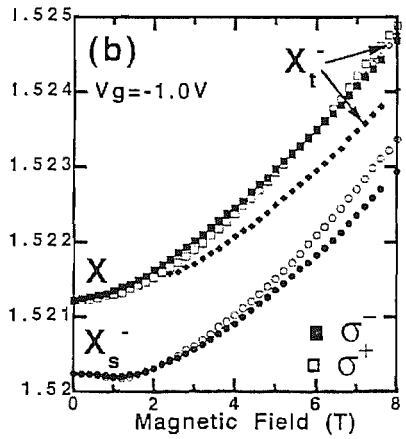

Figure 7.11. Neutral and negatively charged exciton peaks as a function of magnetic field. Note the non-degenerate nature of the negatively charged exciton triplet at high magnetic fields. (Excerpted from Shields et al, (1995).)

The spin dynamics of the negatively charged exciton are considerably more complicated than that of the neutral exciton, because there are now three particles and a total of eight possible spin combinations. The Pauli Exclusion Principle requires that systems with two identical fermions have a total wavefunction which is antisymmetric upon interchange upon interchange of the particles. This is achieved when either the spin part of the wavefunction is symmetric and the spatial part antisymmetric or vice versa. To achieve this the electrons arrange into either a singlet spin state of total spin 0, or a triplet spin state with a total spin quantum number of 1, and z component of

+1, 0 or -1. All the attempts to measure the spin relaxation of negatively charged exciton were taken at the lower energy singlet peak. The combinations of the triplet and singlet states give eight spin states for the negatively charged exciton. Here, only the two spin states for the singlet need concern us. These can be expressed as [4]:

$(1/2^{½})(|e\uparrow,e\downarrow\rangle-|e\downarrow,e\uparrow\rangle)h\uparrow$ and

$(1/2^{½})(|e\uparrow,e\downarrow\rangle-|e\downarrow,e\uparrow\rangle)h\downarrow$

The spin relaxation of the negatively charged exciton is therefore governed solely by spin flip events of the hole. In the neutral exciton, both the electron and the hole undergo spin flip events. This would explain why the spin decay measured at the X^- peak is shorter than that on the X peak, as the spin decay time of holes is considerably shorter.

Analysis of the runs showed nearly all the results required a double exponential fit. i.e., they fitted the equation $A_1\exp[t_1/\ \tau_s] + A_2\exp[t_2/\ \tau_s] + A_3$. However, this was not the case for the measurements taken of the spin decay at the Fermi edge singularity. These measurements fit a single exponential. The 2DEG found at high carrier concentrations only involves, naturally, the spin flip of the electron. Therefore, the high bias values of the spin relaxation measurements fit for a single exponential. The extracted values for spin relaxation time are shown as a function of bias in figures 7.12 (for 10K) and figures 7.13 (for 20K).

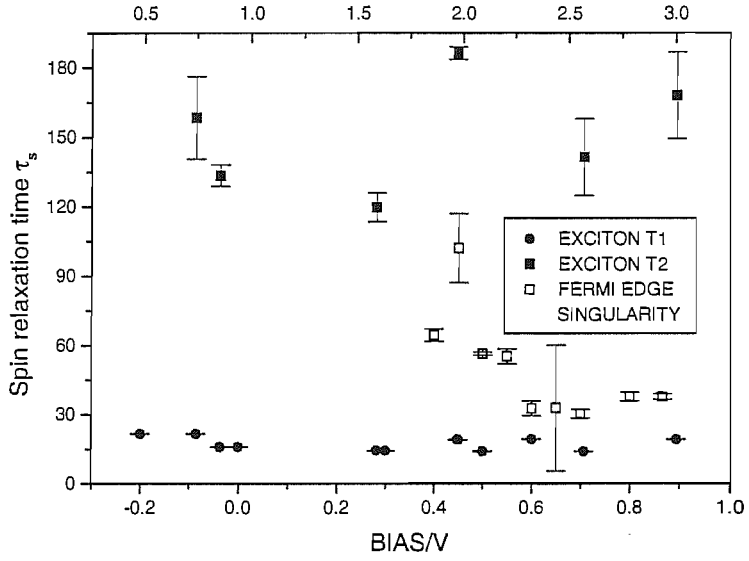

Figure 7.12. Spin relaxation time as a function of bias at 10K.

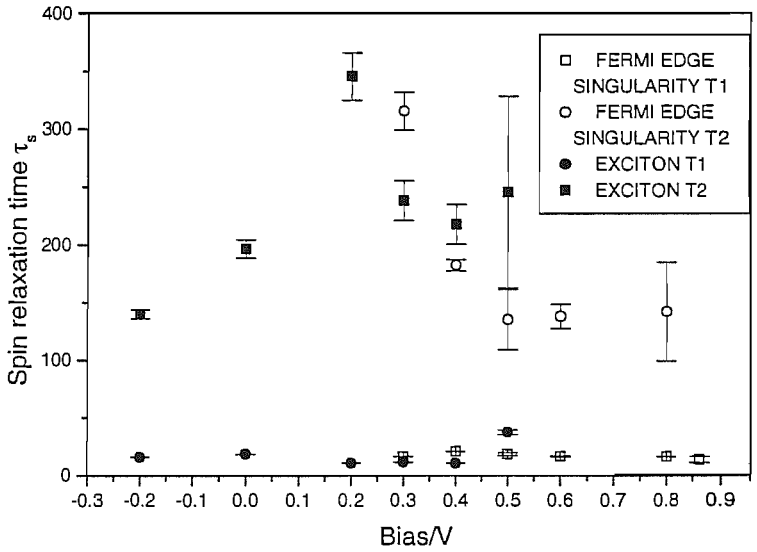

Figure 7.13. Spin relaxation time as a function of bias at 20K.

It was mentioned previously that there are two different spin relaxation mechanisms for the neutral exciton, one involving mutual spin flip of the electron and hole, which is a single exponential process, and individual spin flip of the electron and hole, which is a double exponential process. At first glance these processes seem to be happening in the 10K and 20K runs shown above. However, the spin relaxation seems

to be the opposite of what one would expect. The double exponential fits occur at the lower bias. This is where the electron and hole are close together and the QCSE is weak. One would therefore expect excitonic, single exponential decay to predominate. The difference may be accounted for by considering the possibility of exciton localisation. At temperatures lower than ~ 40K excitons localised within the plane of a quantum well affects spin relaxation mechanisms that are dependent on the wave-vector, for instance the DPK [7] mechanism under discussion here.

If there is interruption of the order of 100 seconds between growth of the well and its barrier layers then the atoms may settle and cause islands of monatomic thickness and a lateral extent of approximately Bohr radius to form. As the confinement energy depends on well width, this leads to different exciton energies in different spatial regions. Such fluctuations in well width provide sites where the dephasing time of excitons is increased. Therefore, mechanisms of spin and radiative decay are strongly influenced by the amount of localisation of the exciton population. However, even if there is no growth interruption and hence no monolayer fluctuations on the interfaces, there are always very short range fluctuations in a system with ternary barriers, due to statistical variations in the alloy composition. In an ideal 2D exciton, the exciton is delocalised over the entire xy plane. The effect of interface roughness on the exciton dynamics depends strongly on the size and depth of the interface islands. When the defect island is of the same magnitude as the exciton Bohr radius, confinement effects due to the defect potential start to become important.

The previously mentioned exchange driven motional narrowing spin relaxation mechanism should be inhibited for strongly localised excitons as their in plane wave vector is small. This would therefore give a double exponential decay, a fast decay corresponding to the localised excitons were the DPK [7] mechanism is

inhibited and a long tail to the spin relaxation corresponding to the delocalised excitons. This would account for the results seen in figures 7.12 and 7.13 above.

7.4 Spin relaxation rate as a function of electron concentration.

As mentioned in the previous section, only the higher biases exhibit evidence of the presence of free electrons. In this section we investigate what deductions are possible about concentration dependence by examining the measurements at high bias values. As may be seen from figures 7.12 and 7.13, only the 10K results show unambiguous evidence of single exponential decay at high bias. Therefore, only the 10K results are of use in determining the concentration dependence. The extracted spin relaxation times are shown in figure 7.14 as a function of bias and in figure 7.15 as a function of concentration.

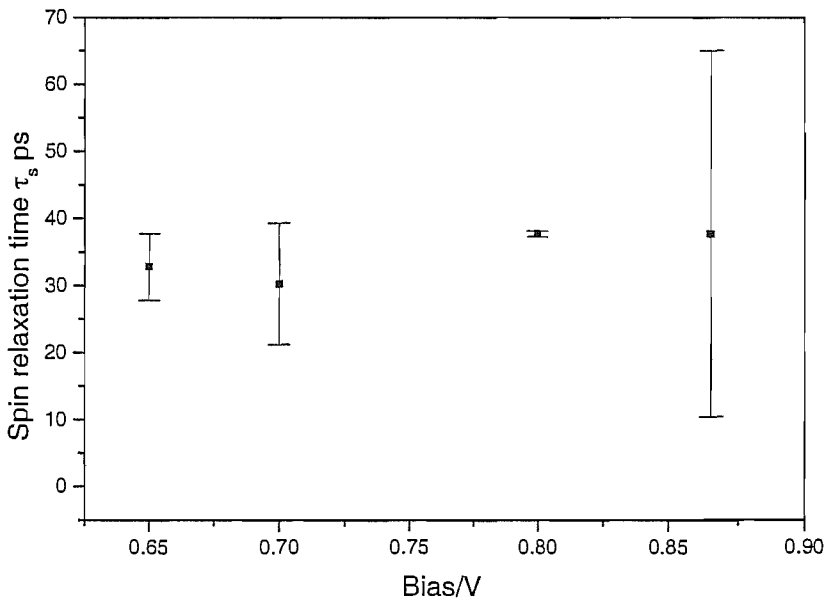

Figure 7.14. Spin decay as a function of bias in the supposed 2DEG region.

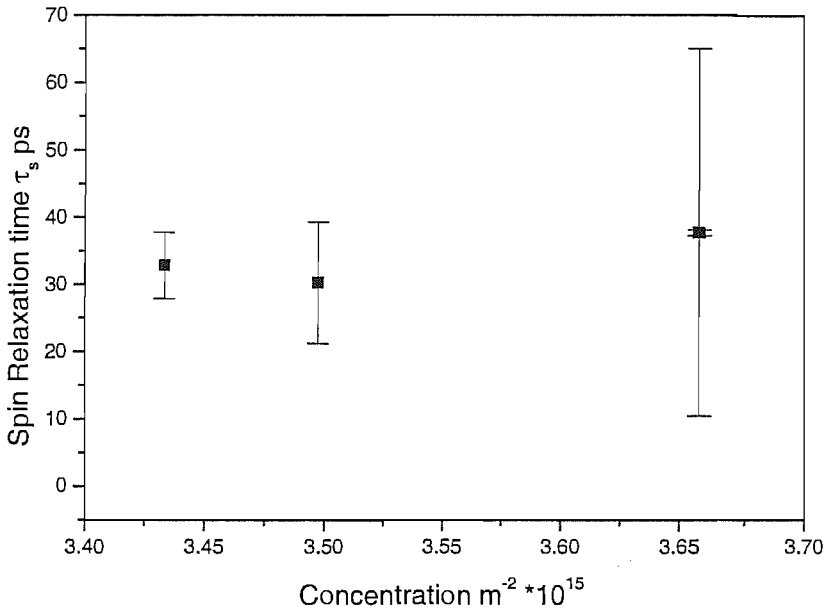

Figure 7.15. Spin decay as a function of electron concentration.

As may be seen above, the concentration stabilises at higher biases. Unfortunately, the region in which unambiguous evidence of free electrons is seen is very narrow in terms of change of concentration and the expected N_s^2 dependence of the spin relaxation cannot be meaningfully investigated.

7.4 Conclusion

This chapter has discussed attempts to investigate the carrier concentration dependence of the spin decay. It was found that, in the case of the 100Å quantum well under investigation, that at carrier concentrations below ~ 10^{15} m^{-2}, excitons predominated in the well. Therefore, it was not viable to discuss spin decay at these concentrations in terms of free electrons.

When measurements at higher concentrations where taken, free electron behaviour was observed. However, there was only limited variation in carrier

concentration and this, combined with the experimental errors, made it difficult to test the hypothesis that the concentration dependence of the spin relaxation rate follows as the square of the electron concentration. For future experiments it is recommended that a sample with higher modulation doping in the barrier be tested. Hopefully such a sample would have a 2DEG across a broader range of biases and hence allow a clear N_s^2 dependence to be observed.

7.5 References.

1. "Lifetime Enhancement of Two-Dimensional Excitons by the Quantum-Confined Stark Effect," H. -J. Polland, L. Schultheis, J. Kuhl, E. O. Göbel and C. W. Tu. Phys. Rev Lett, **55** 2610.

2. "Electron density dependence of the Excitonic absorption thresholds of GaAs quantum wells," R. Kaur, A. J. Shields, J. L. Osbourne, M. Y. Simmons, D. A. Ritchie And M. Pepper. Phys. Stat. Sol. (a) **178**, 465 (2000).

3. "Excess carrier Effects on the Optical emission and excitation Spectra of GaAs Quantum wells," R. Kaur, PhD thesis, Hughes Hall College, University of Cambridge, (2001).

4. "Spin triplet negatively charged excitons in GaAs quantum wells," A. J. Shields, M. Pepper, M. Y. Simmons and D. A. Ritchie, Phys. Rev B, **52** 7841. (1995).

5. "Exciton spin dynamics in quantum wells," M. Z. Maialle, E. A. De Andrada E Silva and L. J. Sham. Phys. Rev B. **47** 15 776. (1993).

6. "Dynamics and spin relaxation of excitons in GaAs/AlxGa1-xAs quantum wells," A. Frommer, A. Ron, E. Cohen, J.A. Kash and L. N. Pfeiffer, Phys. Rev. B, **50** 11 833.

7. Spin relaxation of two-dimensional electrons in noncentrosymmetric semiconductors," M. I. D'yakonov and V. Yu. Kachorovskii, Sov. Phys. Semicond. **20** 110 (1986).

CHAPTER 8

CONCLUSION.

The work detailed in this thesis has shown strong evidence for certain effects in III-V heterostructures. Principally, the work on (110) samples has shown strong evidence of dependence of spin relaxation rate on well growth orientation, namely, that the spin precession may be strongly suppressed when the fictitious magnetic field proposed by the D'yakonov-Perel effect is perpendicular to the plane of the well. It has also been shown that an electric field at right angles to the well plane can be used to gate the spin relaxation and substantially reduced the spin relaxation time.

Work on the (100) sample has shown strong evidence of the contribution of electron-electron scattering to the spin relaxation mechanism in a 2DEG. The main qualitative result is that with electron-electron scattering the spin relaxation rate should have a minimum in the region of T_F and this has been observed. If electron-electron scattering is ignored then the spin-relaxation rate should be considerably greater than observed and follow the temperature dependence of the transport relaxation time.

Further work on this sample was conducted to examine the effect of concentration variation on the spin relaxation rate. While any judgement on this effect must await further data, much interesting work was done on the spin relaxation of excitons (both negatively charged and neutral) and the contribution of localisation to due to growth defects to the spin relaxation. It is suggested that in order to examine concentration dependence a sample that is more heavily modulation doped be used, as this will hopefully increase the voltage range where free electrons are available.

In the course of the work we also investigated use of a magnetic field as a means to separate experimentally the mean square precession frequency and the

electron-electron and transport scattering times in the D'yakonov-Perel spin dynamics. We conclude that application of this idea is not straightforward and will require further work using different samples grown on different crystal orientations before it becomes useful.